THE $^{26}Mg(p,n)^{26}Al$ AND $^{23}Na(\alpha,n)^{26}Al$ REACTIONS

thesis by

Robert Thomas Skelton

In Partial Fulfillment of the Requirements

For the Degree of

Doctor of Philosophy

California Institute of Technology

Pasadena, California

1985

(Submitted October 10, 1984)

ACKNOWLEDGEMENTS

I wish to express my appreciation to the faculty, students, and staff of the W. K. Kellogg Radiation Laboratory for providing an atmosphere wherein research has been not only interesting and exciting, but also fun. In particular I wish to thank Professor R. W. Kavanagh for his patient instruction and guidance, especially when many aspects of this project took more time than anticipated. I am also grateful to Professor W. A. Fowler for his advice and informative discussions, and to Professors C. A. Barnes and S. E. Koonin for their support. Other individuals who have been of particular assistance to me are Professor D. G. Sargood, Dr. H. S. Wilson, Dr. J. L. Osborne, Dr. M. H. Mendenhall, and Dr. J. H. Thomas.

Finally, I want to express my appreciation to my parents, Robert and Mary Skelton, to my sisters, Susan, Rebecca, and Melissa, and to my uncle and aunt, Ted and Louise Carmack, for their understanding and encouragement during this period.

This research was supported in part by the National Science Foundation (PHY79-23638).

ABSTRACT

Cross sections for the $^{26}Mg(p,n)^{26}Al$ reaction have been measured from threshold at $E_p = 4.988$ MeV to $E_p = 5.820$ MeV. Cross sections for the $^{23}Na(\alpha,n)^{26}Al$ reaction have been measured from threshold at $E_\alpha = 3.483$ MeV to $E_\alpha = 4.597$ MeV. In each case separate measurements have been to the ground state and to the first and second excited states of ^{26}Al. Cross sections for the inverse reactions have been calculated and reaction rate factors relating to the destruction of ^{26}Al in a supernova environment have been determined. Astrophysical implications relating to the observation of live and extinct ^{26}Al are discussed. Excitation functions for several additional exit channels for the $^{26}Mg + p$ and $^{23}Na + \alpha$ reactions are reported.

TABLE OF CONTENTS

I. INTRODUCTION

A. ^{26}Al and the Early Solar System

In 1977 Wasserburg and collaborators (Le77) reported large excesses in the $^{26}Mg/^{24}Mg$ isotopic ratio in a Ca-Al rich inclusion in the Allende meteorite. The magnitudes of the excesses in several different chemical phases correlated linearly with the $^{27}Al/^{24}Mg$ ratio, which suggests that the ^{26}Mg resulted from *in situ* decay of ^{26}Al. An alternative possibility is that fossil ^{26}Mg from ^{26}Al decay was mixed into the meteorite from interstellar dust grains, but this would lead to the observed linear correlation only if all of the ^{27}Al present came from the same source as the ^{26}Al. Since this latter possibility is implausible, the conclusion is that the observed excesses are indeed due to *in situ* decay of ^{26}Al; this of course implies that solid objects of macroscopic size (~1cm) condensed on a time scale not long compared to the half-life of ^{26}Al, 7.2×10^5 y (Th84), after completion of nucleosynthesis.

This discovery has generated much interest in models of ^{26}Al production. Explosive nucleosynthesis in supernovae has been examined by Woosley *et al.* (Wo81) and Clayton (Cl82). Their calculations indicate that although the $^{26}Al/^{27}Al$ ratio in the hydrogen-burning shell of a supernova explosion could be as high as 10^{-2}, most of the mass of ^{26}Al is produced in explosive neon burning, so that the overall ratio of $^{26}Al/^{27}Al$ is $\sim1\times10^{-3}$. This ratio is close to that previously obtained by Truran and Cameron (Tr78) and by Arnett and Wefel (Ar78), although in their calculations the ^{26}Al was produced by explosive carbon burning. For both explosive neon burning and explosive carbon burning, the dominant production mechanism for ^{26}Al was the $^{25}Mg(p,\gamma)^{26}Al$ reaction and the dominant

destruction mechanism the $^{26}Al(n,p)^{26}Mg$ reaction. Explosive nucleosynthesis in novae was examined by Woosley and Weaver (Wo80), by Arnould *et al.* (Ar80), and by Hillebrandt and Thielemann (Hi82), who found that the amount of ^{26}Al produced in novae is comparable to that in supernovae, with the lower mass ejected per nova event offset not only by the higher event rate but also by the higher $^{26}Al/^{27}Al$ ratio calculated for novae. This higher ratio (~ 1, according to Hi82) would also permit greater dilution and/or decay prior to meteorite condensation. The possibility that the ^{26}Al in the meteorite resulted after its condensation from spallation reactions from radiations from the early sun has been considered by Lee (Le78a) and found implausible.

A particularly exciting development in the ^{26}Al question has been the recent report of Mahoney *et al.* (Ma82) of detection of the 1809-keV γ-ray characteristic of ^{26}Al decay (see Figure 1) using an orbiting γ-ray detection system aboard the High Energy Astronomical Observatory 3 (*HEAO - 3*). The strength of the line with the detection system looking at the galactic center was $(4.8 \pm 1.0) \times 10^{-4}$ photons/cm^2-sec-sr (Ma84), interpreted as representing $\sim 3 M_\odot$ of ambient ^{26}Al in the interstellar medium. Clayton (Cl84) has re-examined the possibility that this quantity of ^{26}Al arises from galactic supernova contributions. By incorporating among other considerations the latest measurements of the galactic metallicity gradient and time evolution of metallicity in general, he finds that supernovae would need an average $^{26}Al/^{27}Al$ production ratio of $\sim 30 \times 10^{-3}$, 30 times higher than the model estimate. He considers the possibility that the flux arises from a much smaller quantity of ^{26}Al which is much closer, perhaps a single nearby nova or supernova of the recent past ($10^4 - 10^6$ yr). Such a supernova would have to have occurred around 14 parsecs, and a nova around 1 parsec; either event would seem to be unlikely, and Clayton therefore concludes that the most probable source of the observed flux is dispersed nova contributions.

B. Scope of this Experiment

As previously mentioned, the $^{26}Al(n,p)^{26}Mg$ reaction is estimated to be a principal ^{26}Al destruction mechanism in supernovae, but knowledge of the cross section as a function of energy is necessary to compute the reaction rates accurately. Direct measurement of this excitation function is difficult mainly because the target material must be made artificially. However, the values for the $^{26}Al(n_0,p)^{26}Mg$ reaction can be extracted from those of the measurable $^{26}Mg(p,n_0)^{26}Al$ reaction using the principle of detailed balance. (The subscript 0 on the neutron denotes that the nucleus associated with it, namely the ^{26}Al, is in the ground state. Similarly, a subscript of 1 or 2 would denote the first or second excited state of ^{26}Al. ^{26}Mg was used as a target in this experiment, so that only cross sections involving its ground state were studied; the p is therefore understood to be p_0 in this notation.) Reaction rates via the (p,n_0) channel calculated from the experimental data can be compared to those calculated from cross-section values from a theoretical model, such as the Hauser-Feshbach optical model. The extent of agreement can be used to judge the adequacy of the model. Cross sections and reaction rates for the $^{26}Al(n_1,p)^{26}Mg$ and $^{26}Al(n_2,p)^{26}Mg$ reactions, also of interest in nucleosynthesis calculations, are inferred in a similar manner from their inverse reactions. Many of the same experimental techniques developed are equally applicable to the $^{23}Na(\alpha,n)^{26}Al$ reaction, and that reaction was studied in a similar manner.

Thus only those reactions involving the ground state of ^{26}Mg or ^{23}Na were accessible with the materials and techniques available. Reactions involving the excited states of these nuclei are also of interest. Reactions involving the ground state of ^{26}Al can be studied using a target of ^{26}Al, but those involving excited states of nuclei in both channels can only be calculated theoretically.

C. Overview of Experimental Techniques

Figure 1 shows the energy level diagram of ^{26}Al and its decay scheme. Especially to be noted is the isomer level at 228 keV with $J^{\pi}=0^{+}$. This level is the analogue of the ^{26}Mg ground state; its de-excitation by M5 electromagnetic transition is estimated by Moszkowski (Mo55) to have a half-life of $\sim 8\times10^{5}$y, whereas its superallowed β^{+} decay to the ^{26}Mg ground state has a half-life of only 6.35 sec. Since any ^{26}Al ejected in this state will decay to ^{26}Mg long before condensation is possible, it is clearly necessary to consider the first-excited and ground states as separate species in the Mg-Al cycle, the reaction network calculations relating to ^{26}Al production and destruction. Figure 2 shows the most important elements of this network. Among the complications is the possibility of transitions between these two states via inelastic collisions with protons or other light particles. This network is treated by Ward and Fowler (Wa80), emphasizing this last consideration.

In this research project separate measurements were therefore made of the excitation functions to the ground and first two excited states of ^{26}Al in the ^{23}Na$(\alpha,n)^{26}$Al and ^{26}Mg$(p,n)^{26}$Al reactions. Cross sections were determined by bombarding a thin layer of evaporated target material on a substrate with protons or α-particles and counting the number of events leading to the state under examination. The cross section is obtained from the formula:

$$\sigma = 1\times10^{27}\,\frac{Y-B}{\varepsilon\, nt\, N} \qquad (I.1)$$

where σ is the cross section in mb; Y is the total number of events detected; B is the background number of events; ε is the detection efficiency; nt is the target thickness in atoms/cm^2; and N is the number of incident particles. Determination of absolute cross-section data for the various states of ^{26}Al required measurement of the quantities in the above formula; for this several types of detectors and some special target evaporation procedures were used; these are described in detail in Chapter II.

II. EXPERIMENTAL APPARATUS AND PROCEDURES

A. Targets

1. ^{26}Mg Targets

Isotopically enriched ^{26}Mg targets were required in order to avoid difficulties with neutron background from the ^{25}Mg$(p,n)^{25}$Al reaction. 99.7% ^{26}Mg was readily available as MgO, so that a chemical reduction was necessary. The procedure of Takayanagi *et al.* (Ta66) was used; in this procedure, powdered zirconium serves as the reducing agent because the reaction proceeds at ~1200° C, a considerably lower temperature than alternative reducing agents permit. (Tantalum, for example, requires a temperature of ~2000° C.) The reduction was carried out under high vacuum (~10^{-7} torr) in a bell jar. Even at the relatively moderate temperature, the close geometry necessary to utilize the separated isotope efficiently required that the backing be cooled in order that the evaporated magnesium condense on the backing. This was accomplished by maintaining a flow of cooling water on the reverse side of the backing, sealing the cooling water against the high vacuum with an o-ring, as shown in figure 3.

The laboratory threshold energy for the ^{26}Mg$(p,n)^{26}$Al reaction is 4.99 MeV, which is above threshold for many other (p,n) reactions; neutron background from the backing therefore had to be taken into account. The preferred backing material was high purity aluminum foil with a thickness of 0.25 mm, specifically, MARZ grade from Materials Research Inc. The yield from this material was 2500 neutrons/μCoul. at 4.99 MeV. Natural aluminum is isotopically pure (^{27}Al) with a (p,n) threshold of 5.8 MeV, so that the background arose solely from impurities in it. To emphasize the importance of the choice of backing, clean high-purity tungsten was tested and found to yield 14 times as many neutrons for the same beam dose and energy, and at higher energies the disparity became even greater. Slightly lower-purity aluminum (99.999%) yielded 2 to 3 times the neutron rate of the MARZ grade material. For measurements of the cross sections to the second

excited state of ^{26}Mg, a backing of high atomic number became necessary to prevent the 417-keV γ-ray signal from being swamped by higher-energy γ-rays arising from inelastic proton scattering and γ-ray cascades from the ^{27}Al$(p,\gamma)^{28}$Si reaction. The Coulomb barrier associated with the high atomic number inhibits both types of processes. The target used to obtain relative cross sections to this second excited state had in fact been made several years earlier by other researchers in this laboratory (Da79). It consisted of 8.2 μg/cm^2 of ^{26}Mg on a Ta backing 0.25 mm thick; the fact that it had become oxidized did not present any problem since the ^{26}Mg$(p,n_2)^{26}$Al signature, a 417-keV γ-ray line, was well resolved from other γ-ray lines. The relative data were normalized with a different target described below.

Absolute target thickness must be determined in order to obtain an absolute cross section. This was accomplished by Rutherford backscattering, a technique in which accelerated charged particles (α-particles for the cases under discussion) are scattered off the target into some well-defined solid angle and counted with a detector which measures their energy. The differential cross section in the laboratory system is given by Sargood (Sa82):

$$\frac{d\sigma}{d\Omega} = \frac{\left[Z_1 Z_2 e^2(a + \cos\vartheta)\right]^2}{4a\left[E_{lab}\sin^2\vartheta\right]^2} \qquad \text{(II.1)}$$

with the parameter a defined as

$$a = \left[1 - \frac{M_1}{M_2}\sin^2\vartheta\right]^{1/2} \qquad \text{(II.2)}$$

and the other quantities as follows: Z_1, Z_2, M_1, and M_2 are the atomic numbers and nuclear masses of the incident particle and scattering material; e is the electron charge in Gaussian units; and ϑ is the scattering angle in laboratory coordinates. The energy remaining after collision, E^*_{lab}, is given in terms of the incident lab energy, E_{lab}, by

$$\frac{E^*_{lab}}{E_{lab}} = \left[\frac{(M_2^2 - M_1^2 \sin^2 \vartheta)^{1/2} + M_1 \cos \vartheta}{M_1 + M_2} \right]^2 \qquad \text{(II.3)}$$

For the case of ^{26}Mg deposited on ^{27}Al, the target mass is only one unit below the backing mass, so that the backscattering peak for the ^{26}Mg is difficult to separate from the ^{27}Al backscattering edge; this difficulty is further compounded by energy loss in the ^{26}Mg layer. These problems were circumvented by manufacturing a special target on which a 275-μg/cm^2 gold layer was deposited on the aluminum backing, and the ^{26}Mg was deposited on this gold layer. The gold layer was thick enough that energy loss in it reduced the maximum energy of the α-particles scattered by the aluminum below the energy of the α-particles scattered by the ^{26}Mg; at the same time, the gold layer was thin enough that the gold backscattering peak did not intrude onto the ^{26}Mg backscattering peak. The backscattering spectrum for this target is shown in figure 4.

The thickness of other targets was determined by measuring the neutron yield at some convenient proton energy and comparing it to the yield of the special target described in the preceding paragraph. This simple procedure is valid as long as the contribution to the neutron yield from the backing and contaminants is known. This condition was satisfied for the targets on aluminum backings, but not for the one on the Ta backing used for the ^{26}Mg$(p,n_2)^{26}$Al measurements. In order to normalize the data from this target (in effect, to determine the thickness of 8.2 μg/cm^2 stated above), it was necessary to manufacture a separate target. Tungsten had been found to present a lower neutron background than several other heavy metals tested, and a target was evaporated onto a tungsten backing. An identical backing with no ^{26}Mg was prepared and both were bombarded at the selected energy. With the contribution from the backing ($\sim$6%) known, the ^{26}Mg thickness was determined as described above. The energy selected was one at which the ^{26}Mg$(p,n)^{26}$Al was at the maximum of a broad resonance, thus minimizing the fraction of the total yield contributed by the backing. The 417-keV yield from this target was then measured at a

selected bombardment energy in a carefully controlled geometry to deduce the absolute cross section for the $^{26}Mg(p,n_2)^{26}Al$ reaction at that energy; this value was used to normalize the relative data described above.

2. Sodium Targets

Preparation of the sodium targets was simpler than that of the magnesium targets. Natural sodium is isotopically pure (^{23}Na) so it was only necessary to evaporate the selected sodium compound onto the backing. A compound was preferred to avoid the difficulties associated with dealing with highly reactive sodium metal. The first two compounds tested were NaOH and NaCl. High-purity copper foil was selected for backings because both isotopes of copper have relatively high (α,n) thresholds. This combination proved unsatisfactory because both compounds were found to disperse into the copper, so that the energy resolution became extremely poor. Combinations which proved better were $Na_4P_2O_7$ (sodium pyrophosphate) on tungsten and Na_2WO_4 (sodium tungstate) also on tungsten. The tendency to disperse into the backing material was still observed, but to a greatly reduced extent.

One special target for normalizing the relative data by Rutherford backscattering was prepared; it consisted of Na_2WO_4 on a gold backing thin enough (300 $\mu g/cm^2$) that the gold backscattering peak did not extend so low in energy as to interfere with the sodium backscattering peak. Graphite was used to stop the transmitted α beam for the Rutherford backscattering, since α's backscattered from it would not interfere with the sodium peak. Copper was used to stop the transmitted beam for the neutron yield measurement to avoid significant neutron contributions from reactions other than those on the target material. The Rutherford backscattering spectrum from this target is shown in figure 5.

Preliminary investigation showed that the cross section to the 0^+ isomer state of ^{26}Al was generally much less than that to the ground state, in contrast to the situation with $^{26}Mg(p,n)^{26}Al$. This should not be unexpected; even

though the transition to the ground state involves a higher angular momentum barrier ($l = 4$ instead of $l = 2$), the statistical factor, $2J + 1$, favors ground state formation by an 11:1 ratio. No conclusion should be drawn from the $^{26}Mg(p,n_1)^{26}Al$ data since this the target and product nuclei are analogue states. The low cross section necessitated measuring this excitation function with a rather thick target, so that considerable energy resolution was sacrificed. Its thickness was determined in a somewhat complicated manner described in chapter 3.

B. Accelerator, Beam Transport, and Vacuum Systems

1. Negative Ion Source for Proton Beams

Protons are ionized in a Duo-Plasmatron source and accelerated toward an adder canal held at approximately 32 kV. Low pressure H_2 in this canal charge-exchanges with the incident proton beam, and some of it emerges from the canal with a charge of -1, having captured two electrons. The 32 kV then further accelerates these negative ions into a 20° magnet, which bends the beam onto the axis of the tandem accelerator. The proton beam is thus injected into the tandem accelerator with a kinetic energy of approximately 64 keV and a charge of -1, *i.e.*, as H^- ions.

2. JN Accelerator for α-Particle Beams

The Negative Ion Source described above is not well-suited to production of α-particle beams because of the cumbersome lithium oven necessary to produce He^- ions. The α-particle source was instead a model JN single-ended Van de Graaff accelerator, which produces helium ions in a charge state of +1; these ions emerge with an energy of approximately 0.5 MeV and currents up to around 100 μA can be obtained. Before they reach the EN tandem, the ions are neutralized in a canal inside the Negative Ion Source enclosure. The α-particle beam is thus injected into the tandem accelerator with a kinetic energy of approximately 0.5

MeV and electrically neutral.

3. EN Tandem Accelerator

The HVEC Model EN Tandem Accelerator is a Van de Graaff accelerator capable of reaching 6.5 MV at its center terminal. Gas in a stripper canal at this terminal strips electrons from the beam as it reaches that point. H^- ions are therefore accelerated toward the terminal, stripped of both electrons, and accelerated further afterwards; thus they acquire 2 MeV for every MV of terminal voltage. The α-particles, being neutral at injection, are not accelerated approaching the terminal. They are stripped of one or both electrons; some therefore gain 1 MeV/MV and some 2 MeV/MV over their injection energy. Either beam can be used.

4. Beam Optics

The principal element in the beam analyzing system is the 90° analyzing magnet. This magnet isolates only those particles having the correct momentum-to-charge ratio so that the beam exiting the magnet will have a well-defined energy. Several quadrupole and steering magnets are used to control and focus the beam at both high-energy and low-energy ends. At the low-energy end electrostatic elements are also used.

5. Vacuum Systems

Several conventional diffusion pumps, backed by mechanical forepumps, maintain a vacuum of $\sim 10^{-6}$ torr in the beamlines. Two large ion pumps, one at each end of the EN, maintain vacuum in the accelerator column with minimal carbon deposition. (Diffusion pump fluids contain carbon.) Carbon is a serious contaminant in a system where one is examining (p,n) and even more so (α,n) cross sections because of the low threshold and high cross section of ^{13}C for these reactions. The vacuum at the end of the beam line in which the target was mounted was therefore maintained with an ion pump; a cold trap cooled to liquid

nitrogen temperature helped to trap any vapors containing carbon before they could be deposited on the target. A sorption pump, rather than a mechanical pump, was used as a roughing pump to prevent introduction of any vapors containing carbon. Figure 6 shows a schematic of the target chamber arrangement.

C. Sequence Timer

The signature for formation of ^{26}Mg in its 0^+ state is delayed β^+ particle emission with $T_{1/2}$ = 6.35 s. Therefore it is possible to bombard the target for a short time with the β^+ detection system turned off, interrupt the beam, and then measure the β^+ activity for a period of time comparable to the half-life. This procedure avoids a large amount of beam-induced background while maintaining the ability to count a large fraction of the events producing ^{26}Al in its 0^+ state. In practice, several cycles were run, typically 10. A sequence timer originally designed and built by F. M. Mann was used to control steps in the bombard-and-count cycle selected. This device controlled the beam-chopping magnet, a mechanical beam chopper, the neutron-counting scaler gating, the β^+ scaler and/or multichannel analyzer gating, and multichannel analyzer routing. It is described in detail in Mann's thesis (Ma75).

D. Neutron-Detection System

The neutron-detection system consists of a large graphite cube, 12 ^{3}He proportional counters, and the associated electronic equipment.

The graphite cube is approximately 1.4 m on a side and weighs approximately 5000 kg. It is mounted on a cart which moves on rails so that it can be positioned over the end of the beam pipe to place the target at its center. The graphite serves as a neutron moderator; the common isotope of carbon, ^{12}C (98.9%) has a low thermal neutron capture cross section (3.4 mb) so that the thermalized neutrons diffuse around the cube with minimal absorption except by the detectors. (The capture cross section for ^{13}C is even lower, at 0.9 mb.) For

comparison, similar detectors have been constructed out of polyethylene, despite the 330-mb capture cross section of ^{1}H, one of its principal constituents. Such detectors can be made smaller, but their detection efficiency is more strongly dependent on neutron energy.

The 12 ^{3}He gas proportional counters are embedded in the cube near the outside symmetrically located with respect to the center. A gas proportional counter is a tube filled with some particular gas that has a wire running down its axis, the wire being electrically insulated from the tube. High positive voltage is placed on this wire so that electrons produced in the tube are accelerated toward it and positively charged ions toward the outer wall. In a proportional counter, the voltage is high enough that electrons are accelerated sufficiently between collisions to liberate other electrons; the amount of charge reaching the center electrode is therefore much larger than if no gas amplification occurred. The voltage is not so high as to cause the avalanche to saturate; the amount of charge collected is thus proportional to the original number of ion pairs produced by the ionizing event, which in turn is proportional to the energy deposited by the event. A ^{3}He counter detects neutrons via the $^{3}He(n,p)^{3}H$ reaction. This reaction has a cross section of 5300 b at thermal energy and liberates 782 keV to the two resulting charged particles; clearly the p emerges with 75% of this 782 keV and the ^{3}H with the remainder. If both particles deposit their energy within the active region of the volume, the output pulse will correspond to the full energy. If the (n,p) event occurs near the wall, it is possible for the recoiling proton to deposit its energy in the wall, so that only 25% of the energy is deposited in the active volume. The same can occur with the ^{3}H, resulting in deposition of 75% of the energy in the active volume; clearly, either particle could also deposit a fraction of its energy before entering the wall. The anticipated spectrum is therefore a continuous distribution between a threshold at 25% of maximum energy and a spike and cutoff at 100%, with a feature at 75%. Figure 7 shows a spectrum from one of these counters and confirms these expectations.

Each counter is connected to a pre-amplifier which provides impedance matching and amplification to the charge pulse from each counter. Each of the 12 pre-amplifiers delivers its signal to a priority encoder; this device first compares the pulse to the preset threshold value for that particular counter/pre-amplifier combination. If the pulse exceeds the threshold, a pulse is generated which has a height proportional to the counter number. The output of the priority encoder is therefore a series of 12 spikes, the number of counts in a given spike being the number of pulses exceeding the threshold from the corresponding counter. This output could be delivered to a multichannel analyzer to inspect for asymmetries in the neutron distribution or any anomalies in a particular counter. Figure 8 shows the spectrum resulting. Normally, however, only the total number of counts was of interest, and the priority encoder output was simply delivered to a scaler after verifying system performance with a multichannel analyzer.

E. β^+ and γ-Ray Detection Systems

A conventional NaI detector (with photomultiplier tube) was used to count the delayed β^+ particles from the $^{26}Mg(p,n_1)^{26}Al$ reaction, detecting the 511-keV γ-rays resulting from annihilation of the β^+ particles. The target mounting arrangement included a beamtube wall thick enough (~4 mm of aluminum) to stop all the β^+ particles emitted into it; over 90% of the solid angle was subtended; therefore very few β^+ particles annihilated at a large distance from the target. The signal from the photomultiplier was processed by a multichannel analyzer and stored on magnetic tape. The lower count-rates from the $^{23}Na(\alpha,n_1)^{26}Al$ reaction made a more efficient system desirable, and a polystyrene well scintillator to detect the β^+ particles directly was selected. The target was mounted at the end of a thin-walled (0.25 mm stainless steel) beam tube which fit into the well. A schematic of this arrangement is shown in figure 9. The entire assembly was placed inside the graphite cube so that neutrons were counted during the "beam on" segments of the cycle in addition to delayed β^+ particles. A large fraction of

the β^+ particles were emitted with sufficient energy to penetrate the wall and deposit a significant fraction of their energy in the polystyrene. The pulses from its photomultiplier were counted by a scaler with its threshold set to count the bulk of the β^+ distribution and simultaneously by a multichannel analyzer integrating the high energy tail. Use of the scaler data sacrifices some background rejection in favor of counting statistics compared to use of the multichannel analyzer data. A systematic variation was noted in the ratio of the count-rates, suggesting a drift in photomultiplier tube gain. Close analysis shows that the count rate from the bulk of the distribution would be much less sensitive to such a drift than that of the high-energy tail; for the magnitude of the drift calculated, ~3%, it could be ignored compared to other uncertainties. In effect, taking the ratio of count rates for the two different energy "cuts" was a sensitive check for gain drift; a 1% change in count-rate associated with gain drift corresponded to a 5% change in ratio. For both $^{26}Mg(p,n_1)^{26}Al$ and $^{23}Na(\alpha,n_1)^{26}Al$ reactions, a Ge(Li) detection system was used in conjunction with a calibrated ^{22}Na source to determine detection efficiency.

Conventional Ge(Li) systems were also used to detect the 417-keV γ-ray signature from the $^{23}Na(\alpha,n_2)^{26}Al$ and $^{26}Mg(p,n_2)^{26}Al$ reactions. A piece of thin (2 mm) lead sheet was used between the target and Ge(Li) detector; this thickness strongly attenuates low-energy γ-rays, which are copiously emitted by the target under bombardment and by the calibration sources used, but it only moderately reduces γ-rays in the energy range of interest. The signals were processed by a multichannel analyzer and stored on magnetic tape. The Ge(Li) detector was located at 125° with respect to the beam axis in order to measure the total cross section provided that contributing terms in the Legendre polynomial expansion include none above $P_2(\cos\vartheta)$, as indicated by the data of Norman *et al.* (No81a). Detection efficiency was determined by counting calibration sources in a geometry identical to that of the cross-section measurement. Figure 10 shows a spectrum obtained from a ^{152}Eu calibration source, and figure 11

shows a plot of photopeak (full-energy peak) efficiency as a function of γ-ray energy.

III. DATA ANALYSIS

A. Target Yield Formulae

1. Thin Target

When the energy loss of the beam in the target is small compared to the typical resonance width, all interactions can be considered to occur at the same beam energy, and the yield is simply proportional to the target thickness. This state of affairs is the most desirable, as several potential sources of error, discussed below in connection with thick and semi-thick targets, are avoided. The thin-target formula for the cross section is given by equation (I.1); for comparison to the other cases, this formula is re-expressed as

$$Y - B = \frac{\varepsilon N_0 f N_I \sigma t}{A} \qquad \text{(III.1)}$$

where $Y - B$ is the number of events detected over background; ε is the detection efficiency; N_0 is Avogadro's number; f is the number of nuclei of the nuclide under study per molecule of target material; N_I is the number of incident particles; σ is the cross section; t is the thickness in mass per unit area; and A is the molecular weight of the target material.

2. Thick or Semi-Thick Target

A thick target is one which is thick enough that the beam loses sufficient energy within it that it is below threshold for the reaction under study. Typically, the target stops the beam altogether. The yield increases monotonically with increasing beam energy; the yield is proportional to the integral of the cross-section:

$$Y - B = \frac{\varepsilon N_0 f N_I}{A} \int_{E_{th}}^{E_{inc}} \frac{\sigma(E) dE}{\kappa(E)} \qquad \text{(III.2)}$$

where the symbols are defined as above, with a few additions: E_{th} and E_{inc} are threshold and incident energies; σ must now be considered as a function of energy; and κ is the stopping power of the target material, expressed in energy per unit mass-density, *e.g.*, keV/(g/cm^2).

A semi-thick target is the intermediate case in which the energy loss in the target layer is not small compared to the resonance width, but not sufficient to stop the beam. The formula in this case is identical to equation (III.2) except that E_{th} is replaced by E_{ex}, the energy at which the beam exits the back of the target layer. In either of these cases, determination of the actual cross-section values presents not only the mathematical intricacies of unfolding the integrals with the concomitant increased statistical uncertainties, but also an indeterminate uncertainty associated with the distribution of the target material within the target layer; *i.e.* if the distribution is not uniform, the above integrands should be weighted with a function describing the target material concentration within the target layer as a function of depth in the layer.

B. Total Neutron Cross Sections

Analysis of the data for the total neutron cross section was by application of the thin-target formula, equation (I.3). The background count rate for the ^{26}Mg$(p,n)^{26}$Al reaction was determined by bombarding an aluminum foil identical to the backing at various energies. This count rate, ~310 counts (2500 neutrons) per μCoul., corresponded to a cross section of 0.35 mb. For the ^{23}Na$(\alpha,n)^{26}$Al reaction, bombardment of the target below threshold resulted in a yield of 160 counts per μCoul. Resonances in the excitation functions of two common contaminants, ^{18}O and ^{13}C, were examined, and the amount of each was determined; within uncertainties, the contributions from these accounted for all of the yield below threshold. A computer subroutine which incorporated the excitation functions of these two nuclei was written to perform the background subtraction. Typically, the background was ~160 counts/μCoul., corresponding to

0.5 mb; maximum values at a few isolated points were four times these amounts. The neutron-detection efficiency, ε, was determined by measuring the count rate from a ^{252}Cf source which had been calibrated indirectly against a source from the National Bureau of Standards. The detection efficiency measured was $(12.47 \pm 0.40)\%$ for the ^{252}Cf neutron spectrum, which has an average energy of 2.35 MeV. This value was checked by an activation technique. ^{89}Y was bombarded with protons and the neutrons from the ^{89}Y$(p,n)^{89}$Zr reaction were counted. Subsequently, the 909-keV γ-ray activity from the ^{89}Zr was measured with a Ge(Li) system. Since the fraction of ^{89}Zr decays emitting this γ-ray, $(99.01 \pm 0.04)\%$ (Le78b), is accurately known, a straightforward analysis (Sk84) gives the neutron-detection efficiency. Considerable precautions were taken to minimize the possibility of systematic error and to reduce random uncertainties, as this measurement was principally in support of a high-precision measurement of the 478-keV γ-ray branching ratio in the decay of ^{7}Be by Skelton and Kavanagh (Sk84). The neutron-detection efficiency by this technique was $(12.02 \pm 0.08)\%$ for a neutron spectrum with an average energy of 450 keV. The efficiency used for calculations was 12.2%, assumed to be independent of neutron energy as supported by the work of Macklin (Ma57).

The target thickness was measured by Rutherford backscattering of α-particles of 2 MeV incident energy from the special targets described in chapter II at an angle of 160°. The ^{26}Mg thickness was $(36.6 \pm 0.5)\ \mu g/cm^2$; the ^{23}Na thickness was $(1.44 \pm 0.07)\ \mu g/cm^2$. An independent check for the ^{26}Mg was made in connection with the ^{26}Al half-life measurement of Thomas *et al.* (Th84) by measuring the neutron yield from a thick natural magnesium target (99.8%) bombarded with protons at several energies below the threshold for the ^{25}Mg$(p,n)^{25}$Al reaction; the principal source of neutrons was therefore the ^{26}Mg$(p,n)^{26}$Al reaction. The cross sections for (p,n) reactions for most potential chemical impurities are roughly comparable to those measured for ^{26}Mg$(p,n)^{26}$Al, so their contribution to the neutron yield should be $\sim$0.2%; even

if lithium and beryllium were the principal contaminants, their contribution would still be ~4% of the total, but the rarity of these elements renders this possibility remote. This observed yield was compared to the expected yield, calculated by integrating the excitation function and applying the thick-target formula, equation (III.2). An error in the target thickness determined by Rutherford backscattering would result in an inversely proportional normalization error in the cross section, $\sigma(E)$, in this formula; thus the two results would differ by a factor proportional to the error. The observed and calculated yields agreed within 3%; the estimated uncertainty was 5%.

C. Cross Sections to the First Excited State

For the $^{26}Mg(p,n_1)^{26}Al$ reaction, the excitation function was first measured in a constant geometry, but a close one difficult to reproduce to high precision. The resulting data therefore represented the relative cross sections and needed only the cross section measured at a single point to be converted to absolute cross sections. A sample NaI(Tl) spectrum obtained in conjunction with the $^{26}Mg(p,n_1)^{26}Al$ is shown in figure 12. The normalization to absolute cross sections was accomplished by bombarding a target with a large separation (15 cm) between target and detector to minimize the effect of any difference between the positions of the beam spot and the calibration source as well as the effect of the distributed nature of the source. (Positrons have range of ~4mm in aluminum.) A Ge(Li) system was used to measure the annihilation radiation; its detection efficiency was determined with a calibrated ^{22}Na source. The choice of a positron-emitting calibration source, as opposed to a pure γ-ray source, minimized uncertainties arising from the distributed nature of the source and from annihilation in flight. The system detected $(1.68 \pm 0.04) \times 10^{-3}$ annihilation quanta per positron emitted from ^{22}Na. Since only 0.6% of the ^{22}Na positrons annihilate in flight in a low-Z material compared to 4% for those of ^{26m}Al (Ma75), the detection efficiency was $(1.62 \pm 0.04) \times 10^{-3}$ counts in the annihilation photopeak per

positron from ^{26m}Al. The target thickness was determined simply by measuring neutron yield at the peak of the resonance near $E_p = 5.334$ MeV. The yield of 3.00×10^4 counts per μCoul. showed the target thickness to be 25.2 $\mu g / cm^2$. At the peak of this resonance, the cross section was thus determined to be (62.0 $\pm$ 3.0) mb; the dominant source of uncertainty is the reproducibility from one determination to another.

A similar approach was used for the $^{23}Na(\alpha,n_1)^{26}Al$ reaction. Target thickness was again determined by measuring the total neutron yield; however, a much thicker target was found necessary to obtain reasonable counting statistics above background, and the thin-target equation could no longer be used for correlation of the neutron yield to target thickness. This correlation was therefore made by the following procedure. The yield as a function of energy for total neutrons was measured simultaneously with that for the delayed β^+-particles. Previously measured data for the total neutron excitation function from a thin target were integrated by computer over several different energy ranges in order to predict what the yield as a function of energy from this thin target would be if its total amount of ^{23}Na were kept fixed, but if it were distributed uniformly among other materials in the target layer at various concentrations so that energy loss in the target layer would be non-negligible. One result of the target material being distributed in this manner is to degrade the energy resolution. The observed semi-thick target neutron yield as a function of energy was compared to the various predicted functions, and the one presenting the most similar energy resolution was selected. The ratio of neutron yields was then used to infer the total amount of ^{23}Na on the semi-thick target; this amount was 8.9 $\mu g / cm^2$ of ^{23}Na alone, corresponding to 25.7 $\mu g / cm^2$ of $Na_4P_2O_7$. This amount of $Na_4P_2O_7$ corresponds to an energy loss of 18.9 keV in the energy range under consideration; the estimated energy loss in the target was 60 keV, indicating that considerable intermixing of target and backing was occurring, a result not unexpected in view of the high beam currents necessary (~ 1 μA) to obtain

satisfactory yield above background. The energy selected to normalize the relative data was 4.157 MeV, using the same target. The same procedure was used as for the $^{26}Mg(p,n_1)^{26}Al$ described above, with the only difference being that the Ge(Li) detector was considerably closer to the target ($\sim$4 cm) in order to allow for the lower yield. The cross section at this peak was (1.72 $\pm$ 0.17) mb. The detection efficiency was (6.2 $\pm$ 0.2) $\times$ 10^{-3} counts in the annihilation photopeak per ^{26m}Al positron. For the $^{23}Na(\alpha,n_1)^{26}Al$ excitation function, the thin-target formula was used even though the target was much thicker than typical resonances observed in the $^{23}Na(\alpha,n)^{26}Al$ reaction. This procedure can be justified for two reasons. First, the statistical uncertainties and uncertainties arising from the actual ^{23}Na distribution within the target layer are such that an attempt at a more sophisticated analysis would be more a mathematical exercise than a legitimate refinement of the data. Second, and more important, the primary goal in obtaining the data is satisfied nearly as well by making this assumption: to first order, the contribution to $<\sigma v>$, the thermally averaged reaction rate factor (see equation IV.2), from a given resonance depends only on the integral $\int \sigma(E)dE$; use of the thin-target formula for a semi-thick target in effect partially performs this integral so that the same reaction rate is obtained.

One additional factor entered the normalization for the $^{26}Mg(p,n_1)^{26}Al$ and $^{23}Na(\alpha,n_1)^{26}Al$ reactions. In each case, delayed positrons were counted, either directly or via their 511-keV annihilation radiation. Since the detector was turned off while the beam was on, the observed number of counts in equation (III.1) is reduced by a factor f_λ, the fraction of the events which occur during the time that the detection system is sensitive. This factor is given by Bashkin *et al.* (Ba59):

$$f_\lambda = \frac{\exp(-\lambda T_W)\left[1-\exp(-\lambda T_B)\right]\left[1-\exp(-\lambda T_C)\right]}{\lambda T_B\left[1-\exp(-\lambda T_T)\right]} \times$$

$$\left[1-\frac{\left[1-\exp(-m\lambda T_T)\right]}{m\left[\exp(\lambda T_T)-1\right]}\right]. \qquad \text{(III.3)}$$

where the times are defined in figure 13; λ is the decay constant; and m is the total number of cycles. This fraction was approximately 0.5 for all $^{26}Mg(p,n_1)^{26}Al$ and $^{23}Na(\alpha,n_1)^{26}Al$ measurements.

D. Cross Sections to the Second Excited State

As with the first excited state, the approach was to obtain relative data in a close geometry, and then to normalize them in a wide geometry at the peak of a broad resonance. A sample Ge(Li) spectrum for the $^{26}Mg(p,n_2)^{26}Al$ excitation function measurement is shown in figure 14. For the ^{26}Mg, the energy selected for normalization was 5.545 MeV. The γ-ray detection efficiency as a function of γ-ray energy was determined using a ^{152}Eu source; the spectrum and efficiency curve were similar to those shown in figures 10 and 11. The photopeak efficiency at $E_\gamma = 417$ keV was $(0.104 \pm 0.002)\%$. Target thickness was determined by measuring the total neutron yield and subtracting the background from the tungsten backing; the total yield was 5.5×10^5 neutrons per μCoul.; the yield from an identically prepared backing was 1.23×10^5, 22% of the total. The ^{26}Mg thickness was therefore 42.5 $\mu g/cm^2$, resulting in a cross section for $^{26}Mg(p,n_2)^{26}Al$ of (245 ± 7) mb at $E_p = 5.545$ MeV. An independent check was made again in connection with the ^{26}Al half-life measurement of Thomas *et al.* (Th84) by measuring the 417-keV γ-ray yield from a thick natural magnesium target bombarded with protons at energies near the top of the range measured previously. Observed and calculated yields again agreed within 3% with an estimated uncertainty of 5%. For the $^{23}Na(\alpha,n_2)^{26}Al$ reaction, the yield from the backing was much less, and the procedure correspondingly simpler. The Ge(Li) system efficiency was $(1.04 \pm 0.02)\%$ at $E_\gamma = 417$ keV, and the thickness of ^{23}Na was 1.65 $\mu g/cm^2$. This led to an absolute cross section for the

$^{23}Na(\alpha,n_2)^{26}Al$ reaction of (16.1 ± 0.6) mb at $E_\alpha = 4.509$ MeV. Multichannel analyzer spectra were integrated with the TEKHIST computer program. This program allows the user to select three spectral ranges independently: background below and above the peak and the peak itself; the net area is then cross-hatched on the screen and the gross and net integrals displayed and recorded. Further details of the program are given in the thesis of its author, J. L. Osborne (Os83).

IV. RESULTS AND CONCLUSIONS

A. Experimental Results

Figure 15 shows the results of the analysis of the $^{26}Mg(p,n_i)^{26}Al$ data, a preliminary report of which has been made previously (Sk83). The estimated precision for the total neutron data is ±(5% + 0.1) mb; the 5% arises primarily from uncertainties in the overall normalization, while the 0.1 mb arises from uncertainties in background subtraction. The estimated precision for the first-excited-state data is ±(6% + 30 μb); for the second-excited-state data, it is ±(8% + 0.3mb). The excitation function for production of the ground state of ^{26}Al was determined by subtracting the excitation functions for the other two states from the total, and, above the threshold to the first excited state, it is therefore subject to greater uncertainties, given by the quadrature sum of those from the three independent measurements.

Figure 16 shows the results from $^{23}Na(\alpha,n)^{26}Al$. The estimated precision is similarly ±(5% + 0.3mb) for the total neutron data, ±(15% + 5 μb) for the first-excited-state data, and ±(8% + 0.1 mb) for the second-excited-state data. The excitation function to the ground state was determined again by subtraction, and the comment about the uncertainty for the corresponding $^{26}Mg(p,n)^{26}Al$ case applies.

B. Comparison to Previous Experiment

1. $^{26}Mg(p,n)^{26}Al$ Experiments

The first study of the $^{26}Mg(p,n)^{26}Al$ reaction was by Wong *et al.* (Wo67) who investigated it in conjunction with a study of quadrupole deformations; they used time-of-flight to distinguish the neutron groups. However, since their lowest incident proton energy was 8.25 MeV, their results cannot be compared directly to the present experiment.

Furukawa *et al.* (Fu71) bombarded a stacked-foil ^{26}Mg target arrangement with a 52-MeV proton beam and subsequently counted the activity of the long-lived ^{26}Al ($T_{1/2} = 7.2 \times 10^5$ y) with a high-sensitivity detection system; in this manner they determined the cross section for production of the ground state of ^{26}Al. Paul *et al.* (Pa80) bombarded stacked-foil targets at somewhat lower energies (5 to 7 MeV); they subsequently determined the ^{26}Al content of their targets by accelerator mass spectrometry. In both of these experiments, cross sections were measured for production of the ^{26}Al ground state, either directly or via some higher state which decays to the ground state. Within the energy range covered by the present experiment, the only excited state decaying to the ground state is the 417-keV state; these reports are thus to be compared to the sum of the ground state and 417-keV state excitation functions of the present experiment. Figure 17 shows the results of this comparison; only one datum from the first paper and two from the second are within the energy range of the present experiment, but these are seen to agree quite well with the cross-section values measured in the present experiment.

King and Cheng (Ki79) measured the cross section for the ^{26}Mg$(p,n_1)^{26}$Al reaction in a manner similar to that of the present experiment. Figure 18 compares the values they reported to those of the present experiment; their first five points are clearly lower, by factors from 0.5 to 0.8; the sixth point agrees. The discrepancies are well outside estimated uncertainties, suggesting that additional determinations might be appropriate.

Norman *et al.* (No81a) have analyzed the γ-ray yield from a ^{26}Mg target under proton bombardment, with the goal of measuring the total yield to the ground state. Within the energy range of the present experiment, the only contributing state is that of 417 keV; thus the data of their experiment are to be compared to the ^{26}Mg$(p,n_2)^{26}$Al data of the present one. Figure 19 presents both sets of data; the agreement is seen to be excellent.

Norman *et al.* (No81b) have also measured the total neutron yield by using a thick target and analyzing the differential yield to determine the excitation function for the total neutron yield. Figure 20 compares their data to the results of the present experiment; a few isolated points disagree, and it appears that the correction to the effective energy is inconsistent; nevertheless, the overall agreement is again very good.

The thin targets used in the present technique clearly permit much better resolution than was obtained in any of the other experiments. It should however be pointed out that the other experiments spanned greater energy ranges. In general, good energy resolution is not essential in applications for astrophysics because the cross-section data will be averaged for reaction rate calculations; *i.e.*, one calculates the reaction rate factor, $N_0\langle\sigma v\rangle$, where N_0 is Avogadro's number and $\langle\sigma v\rangle$ is given by Fowler *et al.* (Fo67):

$$\langle\sigma v\rangle = \left[\frac{8}{\pi\mu}\right]^{1/2}\left[kT\right]^{-3/2}\int_0^\infty E\sigma(E)\exp(-E/kT)dE. \qquad \text{(IV.1)}$$

Here μ is the system reduced mass; k is the Boltzmann constant; T is the temperature; and E is the center-of-mass system energy. The units of $N_0\langle\sigma v\rangle$ are $cm^3\,mole^{-1}\,sec^{-1}$; one calculates a reaction rate ($cm^{-3}\,sec^{-1}$) by multiplying this factor by the densities of the two reactants. However, for low values of T_9, the lowest resonance (or lowest several resonances) can dominate the integral. (T_9 is the temperature in 10^9 K; $T_9 = 1$ corresponds to a temperature of 10^9 K.) Examples will be given in paragraph C below.

2. $^{23}Na(\alpha,n)^{26}Al$ Experiments

Norman *et al.* (No82) have measured excitation functions for the total neutron yield, the yield to the first excited state, and the yield of various γ-rays at α-particle energies up to 26 MeV using thick-target techniques. Figures 21, 22, and 23 compare cross sections for total neutron yield, first-excited-state production, and second-excited state production respectively. The agreement is

excellent for the total neutron data and for the second-excited-state data; the only point in the first-excited-state data that can be compared is roughly a factor of 2 low compared to the present experiment, suggesting that further investigation of this state may be warranted.

C. Comparison to Theory

The principle of detailed balance allows the cross section for a given reaction to be used to calculate the cross section for the inverse reaction. To invert the cross section for the reaction $0 + 1 \rightarrow 2 + 3$, the formula is given by Fowler *et al.* (Fo67):

$$\frac{\sigma(23 \rightarrow 01)}{\sigma(01 \rightarrow 23)} = \frac{1 + \delta_{23}}{1 + \delta_{01}} \frac{g_0 g_1}{g_2 g_3} \frac{A_0 A_1}{A_2 A_3} \frac{E_{01}}{E_{23}} \qquad \text{(IV.2)}$$

where the δ_{ij} are Kronecker deltas to accommodate the possibility that both particles in either the entrance of exit channel might be identical; the g_i are the spin multiplicities, *i.e.*, $2J_i + 1$; the A_i are the masses; and the E_{ij} are the kinetic energies in the center-of-mass system. This equation was used to calculate the excitation functions for ^{26}Al$(n_i,p)^{26}$Mg leading to the ground state of ^{26}Mg from the lowest three states of ^{26}Al. These results are shown in figure 24, along with the results of a Hauser-Feshbach optical model calculation for comparison. It is clear that the theoretical model considerably overestimates the ^{26}Al$(n_0,p)^{26}$Mg cross section and generally underestimates that of the ^{26}Al$(n_1,p)^{26}$Mg reaction. All cross sections seem to be considerably overestimated at low energies; since the energy denominator in equation (IV.2) can magnify any non-zero cross section arbitrarily, it is possible that ^{26}Mg$(p,n)^{26}$Al cross sections near threshold were below the level detectable and that the ^{26}Al$(n,p)^{26}$Mg cross sections in fact might be much larger at very low energies. However, for energies in the ^{26}Al + n system above 5 keV, the sensitivity of the measurements was sufficient to exclude the theoretical values shown in figure 24. See also the comments below regarding contributions to the reaction rate

factors.

Figure 25 shows the results of applying the principle of detailed balance to the $^{23}Na(\alpha,n)^{26}Al$ data, along with the results of a Hauser-Feshbach calculation. The theory again overestimates the cross section at low energies for the two excited states; for the ground state, the theory underestimates the cross section at nearly all energies.

Tables I and II show the reaction rate factors (equation IV.1) for the $^{26}Al(n_i,p)^{26}Mg$ and $^{26}Al(n_i,\alpha)^{23}Na$ reactions. In calculating these values, the integration was carried out numerically from $E = 0$ to the upper end of the available data. An asymptotic contribution was then added on; this contribution was calculated by assuming a constant value of the cross section above the maximum tabulated value. The asymptotic values were selected by estimating the average cross section over the last 100 keV of experimental data. The values selected were 25, 500, and 50 mb for the $^{26}Al(n_0,p)^{26}Mg$, $^{26}Al(n_1,p)^{26}Mg$, and $^{26}Al(n_2,p)^{26}Mg$ reactions respectively. For the corresponding $^{26}Al(n_i,\alpha)^{23}Na$ reactions the values were 40, 60, and 70 mb. Percentage contributions from the asymptotic term are given in parentheses when they become significant in these tables.

One might suspect that an unlimited contribution to the reaction rate could arise from a small energy denominator in equation IV.2; this is not the case, as the energy denominator is cancelled by the factor of E in the integrand of equation IV.1. Single unobserved resonances near the respective thresholds could add to the tabulated values for the $^{26}Al(n_i,p)^{26}Mg$ reaction rates (table 1) the amounts $N_A \langle \sigma_i v \rangle = 4.7 \times 10^4 T_9^{-3/2}$, $1.6 \times 10^4 T_9^{-3/2}$, and $1.6 \times 10^5 T_9^{-3/2}$ for i = 0, 1, and 2 respectively. For the $^{26}Al(n_i,\alpha)^{23}Na$ reaction rates (table 2) the corresponding coefficients of $T_9^{-3/2}$ are 1.1×10^5, 3.0×10^4, and 6.1×10^4 respectively.

Figures 26 and 27 show the ratios of the reaction rates calculated from the experimental data of figures 24 and 25 to the corresponding reaction rates

calculated using the theoretical cross-section data. The ratios are not plotted for values of T_9 when the contribution from the asymptotic term of the "experimental" reaction rate factor exceeds that from the actual experimental data; this occurs for $T_9 \gtrsim 5$.

The desirability of good experimental resolution is illustrated by the fractional contributions to the $^{26}Al(n_0,p_0)^{26}Mg$ reaction rate factors from the two lowest resonances. At T_9 = 0.1, the resonance at 32 keV in figure 24a contributes approximately 60% of the integral; at T_9 = 0.3, the large resonance at 79 keV contributes a similar percentage. Thus at low temperatures, the exact position and strength of an individual resonance can essentially determine the reaction rate factor.

Table 3 shows several relevant reaction rate factors calculated from the formulae given by Caughlan *et al.* (Ca84). Here the reactions $^{26}Al(n_0,p_t)^{26}Mg$ and $^{26}Al(n_0,\alpha_t)^{23}Na$ refer to *all* states of the product, ground and excited; thus they would not necessarily be comparable to the data of tables 1 and 2. One very significant comparison is however appropriate: the experimentally determined $^{26}Al(n_0,\alpha_0)^{23}Na$ rate is several times the theoretically estimated rate for the $^{26}Al(n_0,\alpha_t)^{23}Na$ reaction. In fact, this experimental $^{26}Al(n_0,\alpha_0)^{23}Na$ reaction rate is a very large fraction (40% to 65%) of the theoretically estimated $^{26}Al(n_0,p_t)^{26}Mg$ rate, the supposed principal destruction mechanism. If higher excited states of ^{23}Na contribute appreciably, it seems possible that $^{26}Al(n,\alpha)^{23}Na$ is in fact the principal destruction mechanism. In any case, the $^{26}Al(n,\alpha)^{23}Na$ reaction clearly contributes significantly to the destruction of ^{26}Al in a neutron-rich environment. These four key reaction rates, the experimental $^{26}Al(n_0,p_0)^{26}Mg$, the experimental $^{26}Al(n_0,\alpha_0)^{23}Na$, the theoretical $^{26}Al(n_0,p_t)^{26}Mg$, and the theoretical $^{26}Al(n_0,\alpha_t)^{23}Na$, are plotted as functions of T_9 in figure 28.

D. Astrophysical Implications

The $^{26}Al(n_0,\alpha_0)^{23}Na$ reaction rates calculated from the data of the present experiment reinforce Clayton's statement (Cl84) that supernovae have little chance of contributing the quantity of ^{26}Al, live and fossil, which has been observed. The alternative suggestion, that contributions from novae dominate, is correspondingly strengthened.

E. Conclusions

Further measurements of reactions involving ^{26}Al are clearly warranted to investigate possible mechanisms for its production and destruction. Several have recently been reported. Champagne (Ch82) has studied the possibility that ^{26}Al production by the $^{25}Mg(p,\gamma)^{26}Al$ reaction might be enhanced by the existence of resonances at low proton energy. Since the Coulomb barrier makes direct study of this reaction infeasible, he has pursued it via the $^{25}Mg(^3He,d)^{26}Al$ reaction and has discovered one candidate level.

The clearest specific need is for direct measurements on ^{26}Al targets to determine the cross sections and reaction rates between various excited states of ^{26}Mg and the ground state of ^{26}Al. Production of such targets has been reported recently by Buchmann *et al.* (Bu84a); also reported has been the use of some of these targets to investigate the $^{26}Al(p,\gamma)^{27}Si$ reaction (Bu84b), a potential destruction mechanism in a proton-rich environment. Trautvetter and Käppeler (Tr84) have very recently reported measurements of the $^{26}Al(n_0,p_1)^{26}Mg$ reaction rate using a neutron spectrum which corresponds to T_9 = 0.29 on a target of ^{26}Al. Reactions to this first excited state of ^{26}Mg ($J^\pi = 2^+$, E = 1.809 MeV) are expected to dominate the rate for $^{26}Al(n_0,p_t)^{26}Mg$. Their result is that $N_0\langle\sigma v\rangle = 6.2\times10^5$ cm^3 mole^{-1} sec^{-1}. This value is remarkably low; it is only 2% of that predicted by Caughlan *et al.* (Ca84) for $^{26}Al(n_0,p_t)^{26}Mg$ and only 25% of the reaction rate for $^{26}Al(n_0,p_0)^{26}Mg$ calculated from the data of the present experiment. This

result, unless contraverted, would permit much greater quantities of ^{26}Al to be produced in a neutron-rich environment, and may resurrect the candidacy of supernovae as the sites for production of the quantities observed.

Further refinement of theoretical models will also be necessary inasmuch as reaction rates involving excited states in both entrance and exit channels are expected to play a significant role. Laboratory measurement of cross-section data between excited states of two nuclei is difficult and complex in favorable cases; for ^{26}Mg and ^{26}Al it would seem to be impossible because of the short life ($\sim$ ps) of the ^{26}Mg excited states and the necessity of a free neutron target if one contemplated use of a beam of ^{26m}Al. One seems therefore obligated to depend on the theoretical calculations for these reactions.

APPENDIX A

As was mentioned in the body of this thesis, when the 417-keV γ-ray yields representing reactions to the second excited state of ^{26}Al were collected, the γ-ray spectra were recorded on magnetic tape. These spectra spanned an energy range from ~300 to 2000 keV; therefore any exit channel from either ^{26}Mg + p or ^{23}Na + α involving emission of a γ-ray in this energy range could be studied with a minor increment of effort. Table 4 lists the reactions for which this has been accomplished; figures 29 through 32 show the results; in each case, the cross section is for the production of the specified γ-ray. Therefore, in order to calculate the cross section to a particular excited state, one must subtract off contributions reaching that state by cascading from a higher one. In all cases the bombarding energy has been converted to excitation energy in the ^{27}Al compound nucleus for use as the abscissa. The principal data of this experiment, the excitation functions for the ^{26}Mg$(p,n_i)^{26}$Al and ^{23}Na$(\alpha,n_i)^{26}$Al reactions, are repeated with this same abscissa. This abscissa was selected to facilitate comparison among all excitation functions measured. The experimental energy ranges covered were E_p = 3.965 to 4.597 MeV for the ^{26}Mg + p entrance channel and E_α = 3.965 to 4.597 MeV for the ^{23}Na + α entrance channel. The formulae for converting the excitation energy to laboratory energy are

$$E_p = 1.03879\, E_{ex} - 8.59151 \qquad \text{(A.1)}$$

and

$$E_\alpha = 1.17411\, E_{ex} - 11.8463 \qquad \text{(A.2)}$$

for the ^{26}Mg + p and ^{23}Na + α entrance channels respectively, where all energies are in MeV.

REFERENCES

Ar78 W. D. Arnett and J. P. Wefel, Astrophysical Journal (Letters) **224**, L139 (1978).

Ar80 M. Arnould, H. Nørgaard, F.-K. Thielemann, and W. Hillebrandt, Astrophysical Journal **237**, 931 (1980).

Ba59 S. Bashkin, R. W. Kavanagh, and P. D. Parker, Physical Review Letters **3**, 518 (1959).

Bu84a L. Buchmann, H. Baumeister, and C. Rolfs, Nuclear Instruments and Methods, *in press*.

Bu84b L. Buchmann, M .Hilgemaier, A. Krauss, A. Redder, C. Rolfs, H. P. Trautvetter, and T. R. Donoghue, Nuclear Physics **A415**, 93 (1984).

Ca84 G. R. Caughlan, W. A. Fowler, M. J. Harris, and B. A. Zimmerman, submitted to Atomic and Nuclear Data Tables (1984).

Ch82 A. E. Champagne, Ph.D. Thesis, Yale University (1982).

Cl82 D. D. Clayton, in *Essays in Nuclear Astrophysics*, edited by C. A. Barnes, D. D. Clayton, and D. N. Schramm (Cambridge: Cambridge University Press), 401 (1982).

Cl84 D. D. Clayton, Astrophysical Journal **280**, 144 (1984).

Da79 J. M. Davidson, D. G. Sargood, and J. L. Zyskind, Bulletin of the American Physical Society **24**, 593 (1979).

Fo67 W. A. Fowler, G. R. Caughlan, and B. A. Zimmerman, Annual Review of Astronomy and Astrophysics **5**, 525 (1967).

Fu71 M. Furukawa, K. Shizuri, K. Komura, K. Sakamoto, and S. Tanaka, Nuclear Physics **A174**, 539 (1971).

Hi82 W. Hillebrandt and F.-K. Thielemann, Astrophysical Journal **255**, 617 (1982).

Ki79 J. D. King and C. W. Cheng, Canadian Journal of Physics **57**, 286 (1979); erratum, Canadian Journal of Physics **57**, 1063.

Le77 Typhoon Lee, D. A. Papanastassiou, and G. J Wasserburg, Astrophysical Journal (Letters) **211**, L107 (1977).

Le78a Typhoon Lee, Astrophysical Journal **224**, 217 (1978).

Le78b *Table of the Isotopes (7th ed.)*, edited by C. M. Lederer and V. S. Shirley (New York: John Wiley and Sons) (1978).

Ma57 R. L. Macklin, Nuclear Instuments **1**, 335 (1957).

Ma75 F. M. Mann, Ph.D. Thesis, California Institute of Technology (1975).

Ma82 W. A. Mahoney, J. C. Ling, A. S. Jacobson, and R. E. Lingenfelter, Astrophysical Journal **262**, 742 (1982).

Ma84 W. A. Mahoney, J. C. Ling, W. A. Wheaton, and A. S. Jacobson, Astrophysical Journal, *in press* (1984).

Me78 R. A. Meyer, *Multigamma-Ray Calibration Sources* (Booklet M-100), (Livermore, California: University of California) (1978).

Mo55 S. A. Moszkowski, in *Beta- and Gamma-Ray Spectroscopy*, ed. K. Siegbahn (New York: Interscience), chap. 13, p. 391 (1955).

No81a E. B. Norman, K. T. Lesko, T. E. Chupp, and P. Schwalbach, Nuclear Physics **A357**, 228 (1981).

No81b E. B. Norman, T. E. Chupp, K. T. Lesko, and P. J. Grant, Astrophysical Journal **251**, 834 (1981).

No82 E. B. Norman, T. E. Chupp, K. T. Lesko, P. Schwalbach, and P. J. Grant, Nuclear Physics **A390**, 561 (1982).

Os83 J. L. Osborne, Ph.D. Thesis, California Institute of Technology (1983).

Pa80 M. Paul, W. Henning, W. Kutschera, E. J. Stephenson, and J. L. Yntema, Physics Letters **94B**, 303 (1980).

Sa82 D. G. Sargood, Physics Reports **93**, 62 (1982).

Sk83 R. T. Skelton, R. W. Kavanagh, and D. G. Sargood, Astrophysical Journal **271**, 404 (1983); erratum (submitted).

Sk84 R. T. Skelton and R. W. Kavanagh, Nuclear Physics **A414**, 141 (1984).

Ta66 S. Takayanagi, M. Katsuta, K. Katori, and R. Chiba, Nuclear Instruments and Methods **45**, 345 (1966).

Th84 J. H. Thomas, R. L. Rau, R. T. Skelton, and R. W. Kavanagh, Physical Review **C30**, 385 (1984).

Tr78 J. W. Truran and A. G. W. Cameron, Astrophysical Journal **219**, 226 (1978).

Tr84 H. P. Trautvetter and F. Käppeler, Zeitschrift für Physik, *in press*.

Wa80 R. A. Ward and W. A. Fowler, Astrophysical Journal **238**, 266 (1980).

Wo67 C. Wong, J. D. Anderson, J. W. McClure, and B. Pohl, Physics Review **156**, 1266 (1967).

Wo80 S. E. Woosley and T. A. Weaver, Astrophysical Journal **238**, 1017 (1980).

Wo81 S. E. Woosley, T. S. Axelrod, and T. A. Weaver, Comments on Nuclear and Particle Physics **9**, 185 (1981).

TABLE 1

^{26}Al $(n_i, p_0)^{26}$Mg Experimental Reaction Rate Factors

The reaction rate factors, $N_0 \langle \sigma_i v \rangle$, for reactions from the three lowest states of ^{26}Al to the ground state of ^{26}Mg. The values are calculated from data of the present experiment. Asymptotic cross sections are used for cross sections above the experimental range. The numbers in parentheses represent the percentage contributions from the asymptotic term.

TABLE 1

T_9	$^{26}Al(n_0,p_0)^{26}Mg$	$^{26}Al(n_1,p_0)^{26}Mg$	$^{26}Al(n_2,p_0)^{26}Mg$
0.10	2.32 E+05	2.64 E+07	1.25 E+07
0.15	4.95 E+05	4.10 E+07	2.22 E+07
0.20	8.30 E+05	6.07 E+07	3.21 E+07
0.30	1.51 E+06	1.10 E+08	5.03 E+07
0.40	2.05 E+06	1.57 E+08	6.53 E+07
0.50	2.46 E+06	1.94 E+08	7.60 E+07
0.60	2.79 E+06	2.22 E+08	8.28 E+07
0.70	3.07 E+06	2.44 E+08	8.65 E+07
0.80	3.31 E+06	2.60 E+08	8.81 E+07
0.90	3.53 E+06	2.74 E+08	8.83 E+07 (1)
1.00	3.73 E+06	2.85 E+08	8.75 E+07 (1)
1.50	4.49 E+06 (3)	3.26 E+08 (3)	7.84 E+07 (4)
2.00	5.21 E+06 (10)	3.53 E+08 (8)	6.93 E+07 (9)
2.50	6.04 E+06 (20)	3.71 E+08 (15)	6.27 E+07 (16)
3.00	6.98 E+06 (31)	3.84 E+08 (21)	5.80 E+07 (23)
3.50	7.98 E+06 (41)	3.94 E+08 (28)	5.48 E+07 (30)
4.00	9.02 E+06 (49)	4.03 E+08 (34)	5.26 E+07 (36)
4.50	1.00 E+07 (56)	4.11 E+08 (40)	5.11 E+07 (42)
5.00	1.11 E+07 (62)	4.19 E+08 (45)	5.02 E+07 (48)
6.00	1.30 E+07 (71)	4.35 E+08 (54)	4.93 E+07 (57)
7.00	1.48 E+07 (77)	4.51 E+08 (61)	4.94 E+07 (65)
8.00	1.64 E+07 (81)	4.67 E+08 (67)	5.00 E+07 (70)
9.00	1.80 E+07 (84)	4.83 E+08 (72)	5.09 E+07 (75)
10.00	1.94 E+07 (87)	5.00 E+08 (76)	5.20 E+07 (79)

TABLE 2

$^{26}Al(n_i,\alpha_0)^{26}Mg$ Experimental Reaction Rate Factors

The reaction rate factors, $N_0 \langle \sigma_i v \rangle$, for reactions from the three lowest states of ^{26}Al to the ground state of ^{23}Na. The values are calculated from data of the present experiment. Asymptotic cross sections are used for cross sections above the experimental range. The numbers in parentheses represent the percentage contributions from the asymptotic term.

TABLE 2

T_9	$^{26}Al(n_0,\alpha_0)^{23}Na$	$^{26}Al(n_1,\alpha_0)^{23}Na$	$^{26}Al(n_2,\alpha_0)^{23}Na$
0.10	2.08 E+07	2.37 E+06	4.10 E+06
0.15	1.69 E+07	2.94 E+06	5.42 E+06
0.20	1.50 E+07	4.25 E+06	7.39 E+06
0.30	1.34 E+07	7.40 E+06	1.13 E+07
0.40	1.31 E+07	1.00 E+07	1.42 E+07
0.50	1.31 E+07	1.18 E+07	1.63 E+07
0.60	1.33 E+07	1.31 E+07	1.79 E+07
0.70	1.36 E+07	1.40 E+07	1.92 E+07
0.80	1.38 E+07	1.48 E+07	2.03 E+07
0.90	1.40 E+07	1.55 E+07	2.13 E+07 (1)
1.00	1.42 E+07	1.61 E+07	2.22 E+07 (1)
1.50	1.53 E+07 (1)	1.92 E+07 (3)	2.59 E+07 (8)
2.00	1.66 E+07 (3)	2.22 E+07 (9)	2.92 E+07 (18)
2.50	1.80 E+07 (7)	2.50 E+07 (16)	3.22 E+07 (28)
3.00	1.95 E+07 (12)	2.77 E+07 (25)	3.50 E+07 (38)
3.50	2.09 E+07 (18)	3.01 E+07 (33)	3.75 E+07 (46)
4.00	2.22 E+07 (24)	3.24 E+07 (40)	4.00 E+07 (54)
4.50	2.35 E+07 (30)	3.46 E+07 (46)	4.23 E+07 (59)
5.00	2.48 E+07 (36)	3.66 E+07 (52)	4.45 E+07 (64)
6.00	2.71 E+07 (46)	4.04 E+07 (61)	4.86 E+07 (72)
7.00	2.93 E+07 (54)	4.38 E+07 (68)	5.24 E+07 (77)
8.00	3.14 E+07 (61)	4.70 E+07 (73)	5.59 E+07 (82)
9.00	3.33 E+07 (66)	5.00 E+07 (77)	5.93 E+07 (85)
10.00	3.52 E+07 (71)	5.28 E+07 (81)	6.24 E+07 (87)

TABLE 3

^{26}Al Theoretical Reaction Rate Factors

The total reaction rate factors, $N_0 \langle \sigma v \rangle$ for reactions from the ground state and the first excited state of ^{26}Al to any state of ^{26}Mg and ^{23}Na. These are the theoretical reaction rates from the parametrized formulation of Caughlan *et al.* (Ca84).

TABLE 3

T_9	$^{26}Al(n_0,p_t)^{26}Mg$	$^{26}Al(n_1,p_t)^{26}Mg$	$^{26}Al(n_0,\alpha_t)^{23}Na$	$^{26}Al(n_1,\alpha_t)^{23}Na$
0.10	3.10 E+07	1.30 E+07	6.98 E+06	1.44 E+07
0.15	3.12 E+07	2.30 E+07	6.46 E+06	1.44 E+07
0.20	3.13 E+07	3.52 E+07	6.14 E+06	1.44 E+07
0.30	3.16 E+07	6.74 E+07	5.87 E+06	1.44 E+07
0.40	3.19 E+07	1.02 E+08	5.90 E+06	1.44 E+07
0.50	3.22 E+07	1.32 E+08	6.11 E+06	1.44 E+07
0.60	3.24 E+07	1.56 E+08	6.45 E+06	1.44 E+07
0.70	3.26 E+07	1.76 E+08	6.89 E+06	1.44 E+07
0.80	3.27 E+07	1.91 E+08	7.40 E+06	1.44 E+07
0.90	3.28 E+07	2.04 E+08	7.98 E+06	1.44 E+07
1.00	3.29 E+07	2.13 E+08	8.61 E+06	1.44 E+07
1.50	3.34 E+07	2.37 E+08	1.23 E+07	1.45 E+07
2.00	3.49 E+07	2.43 E+08	1.67 E+07	1.53 E+07
2.50	3.77 E+07	2.42 E+08	2.15 E+07	1.73 E+07
3.00	4.17 E+07	2.38 E+08	2.65 E+07	2.07 E+07
3.50	4.69 E+07	2.33 E+08	3.17 E+07	2.56 E+07
4.00	5.29 E+07	2.29 E+08	3.69 E+07	3.21 E+07
4.50	5.99 E+07	2.24 E+08	4.22 E+07	4.00 E+07
5.00	6.75 E+07	2.19 E+08	4.75 E+07	4.94 E+07
6.00	8.39 E+07	2.10 E+08	5.81 E+07	7.21 E+07
7.00	9.94 E+07	2.02 E+08	6.86 E+07	9.90 E+07
8.00	1.10 E+08	1.95 E+08	7.90 E+07	1.29 E+08
9.00	1.12 E+08	1.88 E+08	8.95 E+07	1.61 E+08
10.00	1.02 E+08	1.83 E+08	9.99 E+07	1.94 E+08

TABLE 4

Summary of Excitation Functions

This tabulation provides a summary and index for the excitation functions of all exit channels analyzed from ^{26}Mg + p and ^{23}Na + n; the ^{26}Al + n exit channels are included for comparison. See Appendix A.

TABLE 4

Summary of Excitation Functions

Reaction	γ-Ray Energy (keV)	Figure
$^{26}Mg(p,n_0)^{26}Al$		29a
$^{26}Mg(p,n_1)^{26}Al$		29b
$^{26}Mg(p,n_2)^{26}Al$	417	29c
$^{26}Mg(p,n_t)^{26}Al$		29d
$^{23}Na(\alpha,n_0)^{26}Al$		30a
$^{23}Na(\alpha,n_1)^{26}Al$		30b
$^{23}Na(\alpha,n_2)^{26}Al$	417	30c
$^{23}Na(\alpha,n_t)^{26}Al$		30d
$^{26}Mg(p,p')^{26}Mg^*$	1809	31a
$^{26}Mg(p,p')^{26}Mg^*$	1130	31b
$^{26}Mg(p,p')^{26}Mg^*$	1779	31c
$^{26}Mg(p,p')^{26}Mg^*$	1003	31d
$^{26}Mg(p,\alpha_1)^{23}Na^*$	440	32a
$^{23}Na(\alpha,\alpha')^{23}Na^*$	440	32b
$^{23}Na(\alpha,p)^{26}Mg^*$	1809	32c

FIGURE 1

Energy Level Structure and Decay Scheme of ^{26}Al

All energies are shown to scale. The entrance levels for the two reactions studied, ^{26}Mg$(p,n)^{26}$Al and ^{23}Na$(\alpha,n)^{26}$Al, are shown at the right. The vertical scales show excitation energy in the center-of-mass system for each case; the energy regions for which data were obtained are indicated by the vertical bars.

FIGURE 1

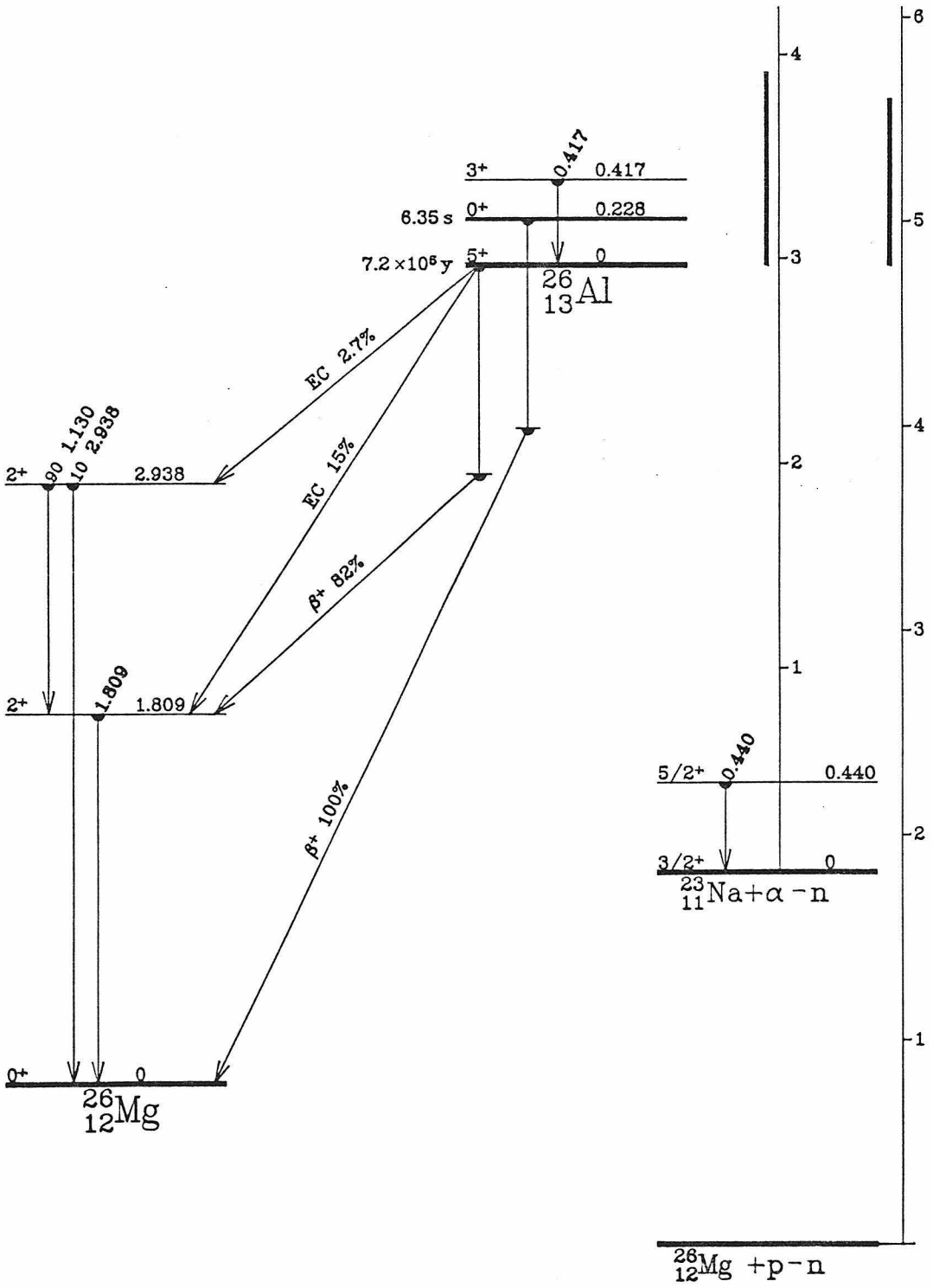
3+
0.417
0.417
6.35 s
0+
0.228
7.2×10⁵ y
5+
0
26 13Al
EC 2.7%
EC 15%
β+ 82%
β+ 100%
2+
90 1.130
10 2.938
2.938
2+
1.809
1.809
0+
0
26 12Mg
5/2+
0.440
0.440
3/2+
0
23 11Na+α−n
26 12Mg +p−n
6
5
4
3
2
1
4
3
2
1

FIGURE 2

The Mg-Al Cycle

The dominant net effect of the cycle is to convert 4 protons into the α-particle, emerging from the $^{27}Al(p,\alpha)^{24}Mg$ reaction; the isotopes of Mg and Al act as catalysts. Nuclei reaching A = 28 escape from the cycle. Half-lives for β^+ emission are shown. $^{26}Al(n,p)^{26}Mg$ paths are the same as those for β^+ emission by ^{26}Al. (After Wa80).

FIGURE 2

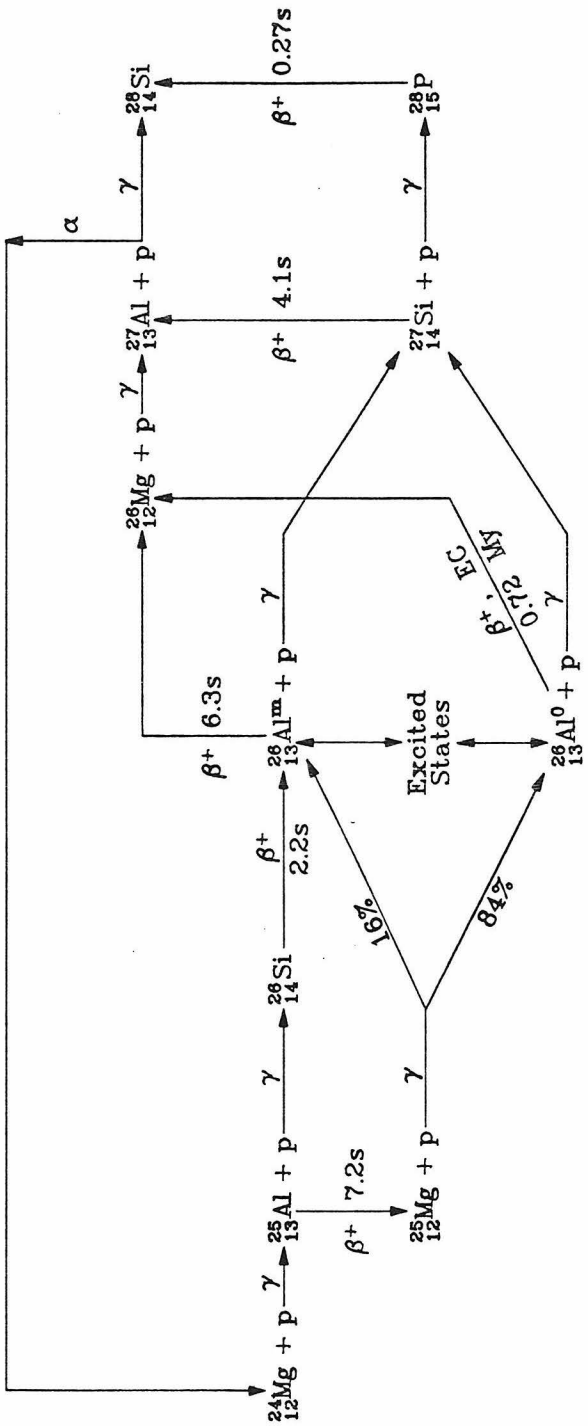
$^{24}_{12}Mg + p$
γ
$^{25}_{13}Al + p$
β^+ 7.2s
$^{25}_{12}Mg + p$
γ
$^{26}_{14}Si$
β^+ 2.2s
$^{26}_{13}Al^m + p$
β^+ 6.3s
$^{26}_{12}Mg + p$
γ
$^{27}_{13}Al + p$
α
$^{28}_{14}Si$
γ
$^{28}_{15}P$
β^+ 0.27s
$^{27}_{14}Si + p$
β^+ 4.1s
γ
$^{26}_{13}Al^0 + p$
γ
EC
β^+, M
0.712
Excited States
16%
84%
γ
$^{25}_{12}Mg + p$

FIGURE 3

Water-Cooled Target Mount

This arrangement was used for manufacturing the ^{26}Mg targets by reduction of MgO with zirconium powder. A current of several hundred amperes flowing through the evaporation boat was used to heat the materials in it to a temperature sufficient for the reaction to proceed ($\sim$1200° C). The liberated ^{26}Mg would then evaporate and condense on the cooled target backing. To furnish an approximate size scale, the exposed aperture of the target backing was 13 mm.

FIGURE 3

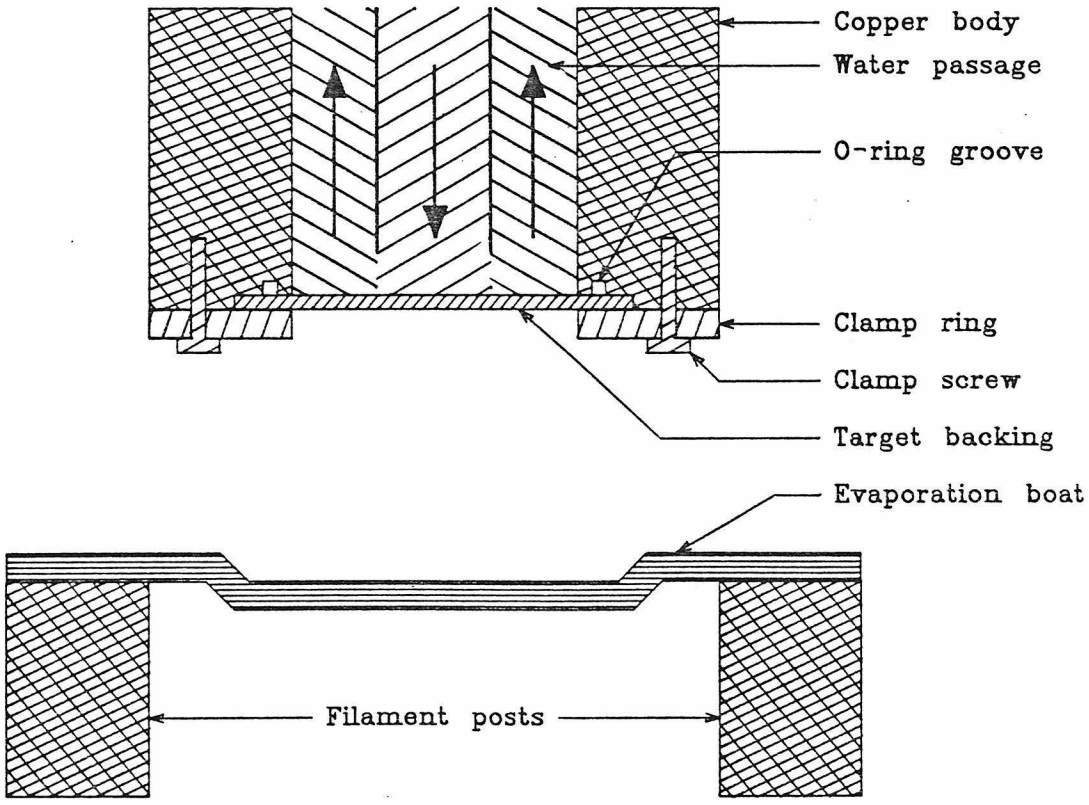
Copper body
Water passage
O-ring groove
Clamp ring
Clamp screw
Target backing
Evaporation boat
Filament posts

FIGURE 4

Rutherford Backscattering for ^{26}Mg Thickness Measurement

Figure 4a was obtained from a target consisting of ^{26}Mg on a thin gold substrate on an aluminum backing bombarded with 2-MeV α-particles. The features of this spectrum are the backscattering edge from the aluminum backing (1), the peak from the ^{26}Mg (2), and the peaks from the gold (3 and 4). The main gold peak (3) represents backscattering of α-particles which traversed the ^{26}Mg layer; the minor peak (4) represents backscattering from gold on the front surface, probably indicating a pinhole in the ^{26}Mg layer. Figure 4b was obtained from a comparison target which had a gold layer on aluminum, but no ^{26}Mg. This spectrum was obtained with geometry and electronics identical to those of figure 4a. The two principal features are the aluminum edge (1) and the gold peak (2). Comparison of the two spectra shows the energy suppression of the gold edge by the ^{26}Mg as well as the further suppression of the aluminum edge by the ^{26}Mg. (Even in figure 4b the aluminum edge is being suppressed by energy loss in the gold. Backscattering from aluminum on the front surface would produce an edge at an energy slightly higher than that of the ^{26}Mg peak in figure 4a; in practice the two would merge because the resolution of the detector would not be sufficient to separate them.)

FIGURE 4

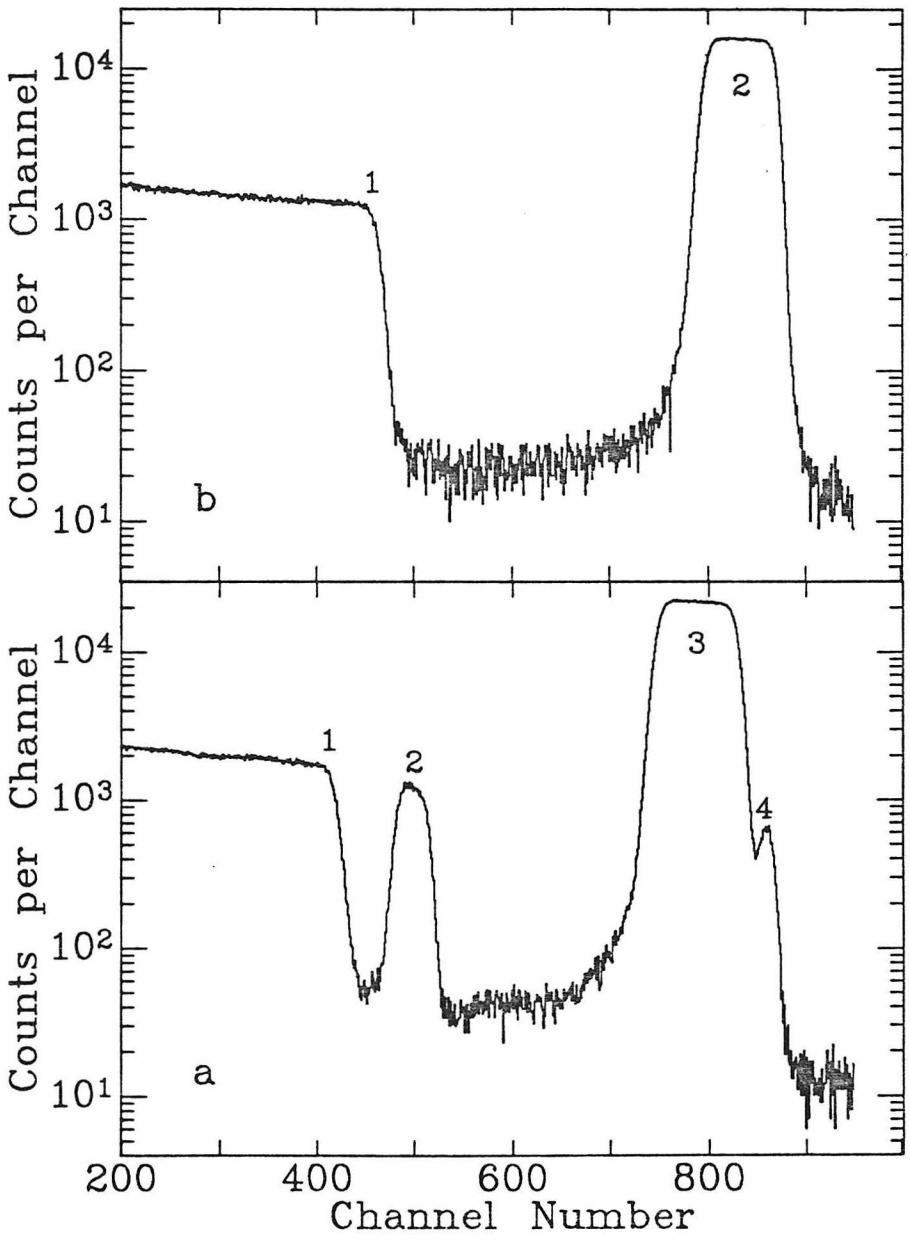
Counts per Channel
10^4
10^3
10^2
10^1
1
2
b
Counts per Channel
10^4
10^3
10^2
10^1
1
2
3
4
a
200
400
600
800
Channel Number

FIGURE 5

Rutherford Backscattering for ^{23}Na Thickness Measurement

The target was Na_2WO_4 on a thin gold foil with a graphite beam stop; it was bombarded with 2-MeV α-particles. The features of this spectrum are the graphite beam-stop edge (1) and peaks from a small amount of surface carbon (2), from oxygen (3), from ^{23}Na (4), and from the gold and tungsten (5).

FIGURE 5

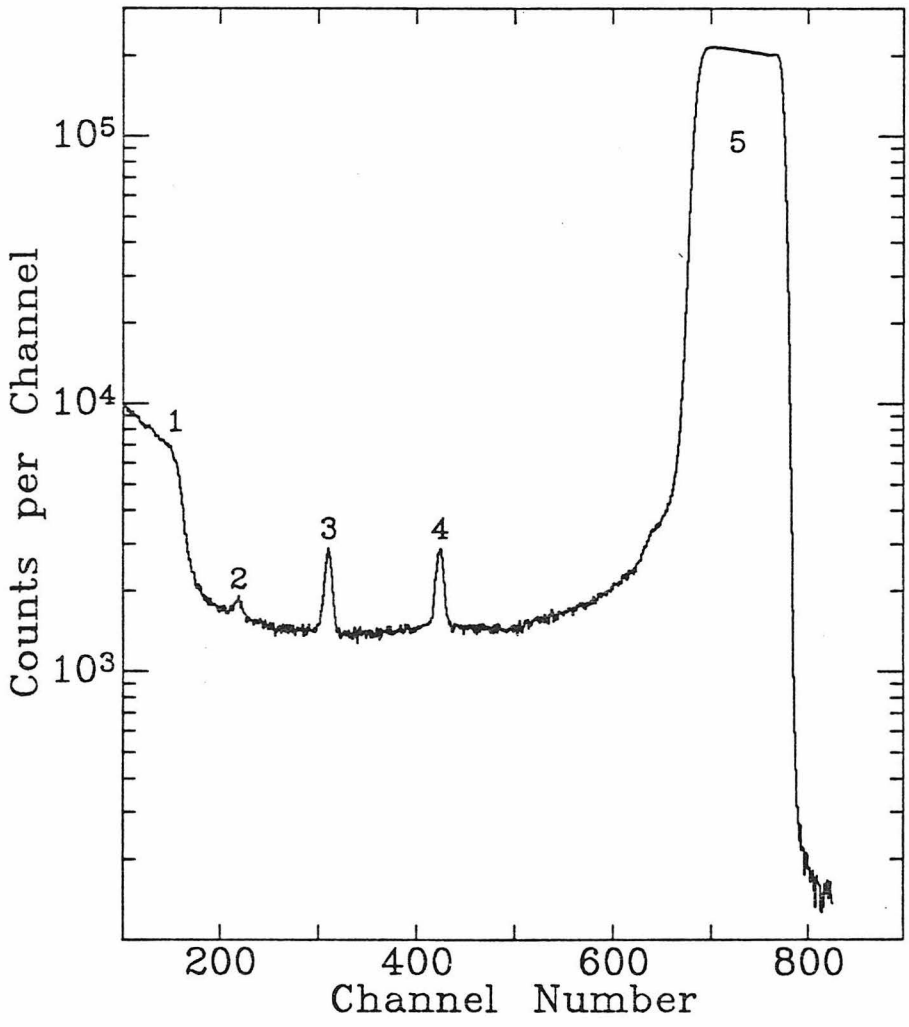
Counts per Channel
10^5
10^4
10^3
1
2
3
4
5
200
400
600
800
Channel Number

FIGURE 6

Target Chamber

The cold trap minimized the amount of carbon-containing vapors entering from the upstream side. The beam was defined by the aperture, 5 mm in diameter. The last 77 cm of beam tube acted as a Faraday cup.

FIGURE 6

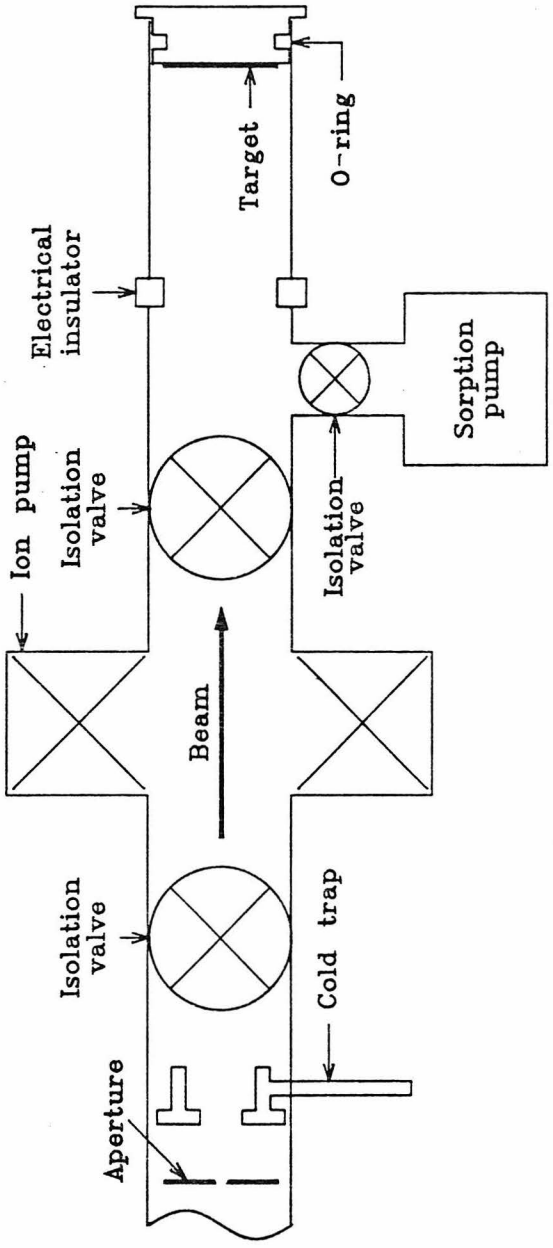
Target
O-ring
Electrical insulator
Sorption pump
Ion pump
Isolation valve
Isolation valve
Beam
Isolation valve
Cold trap
Aperture

FIGURE 7

Output Spectrum from a ^{3}He Detector

Features of this spectrum are the threshold at 25% of full energy associated with the proton entering the wall (1), the break associated with the ^{3}H entering the wall (2), and the full-energy peak (3). The threshold would be set around channel 100. (See text).

FIGURE 7

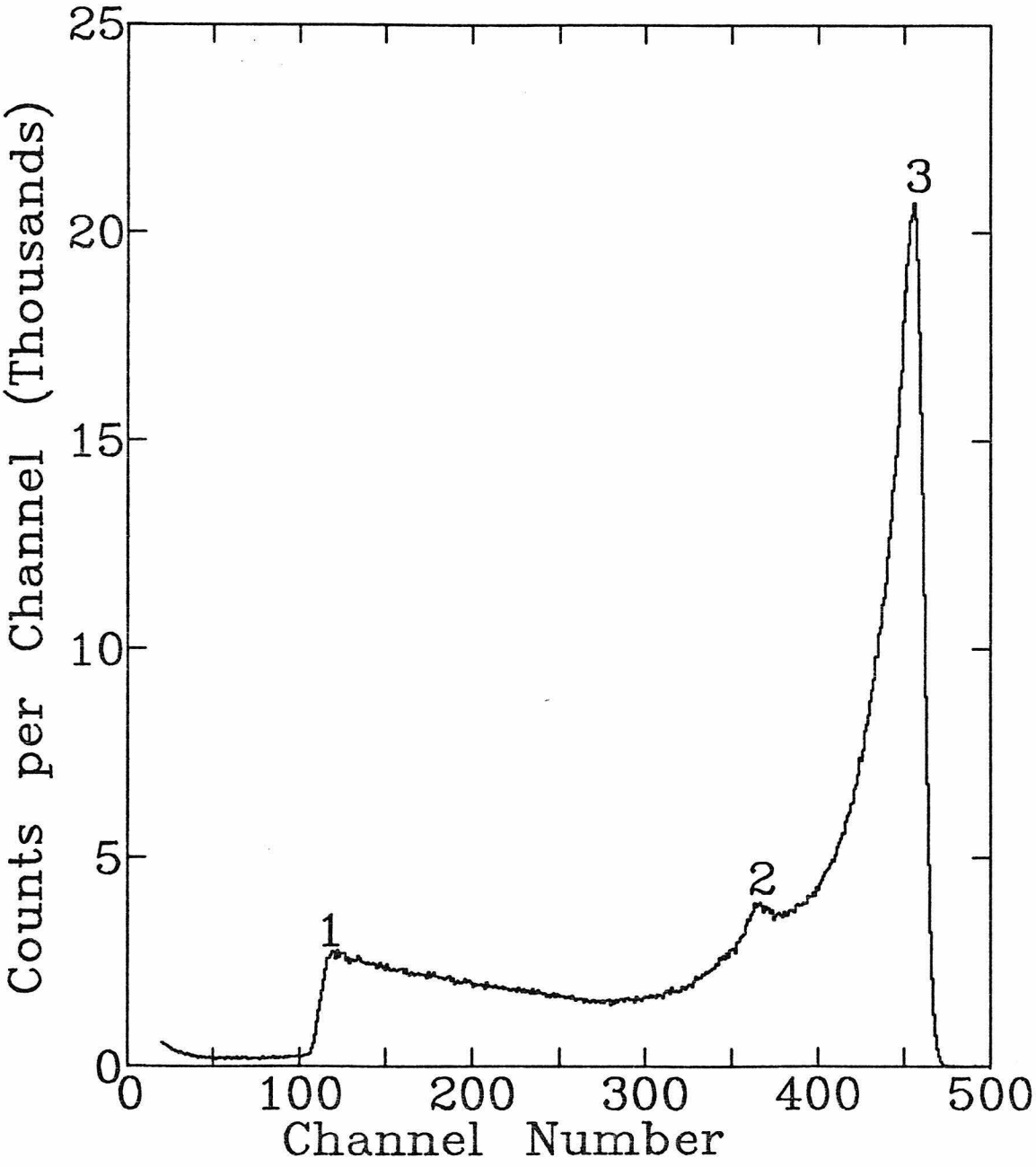
Counts per Channel (Thousands)
25
20
15
10
5
0
0
100
200
300
400
500
Channel Number
1
2
3

FIGURE 8

Output from the Priority Encoder

Each "spike" represents one of the 12 counters. The pulses from channels 7 and 8 are more closely spaced because of details of the circuit design; since their separation still exceeds any reasonable requirement, no attempt to improve this was made.

FIGURE 8

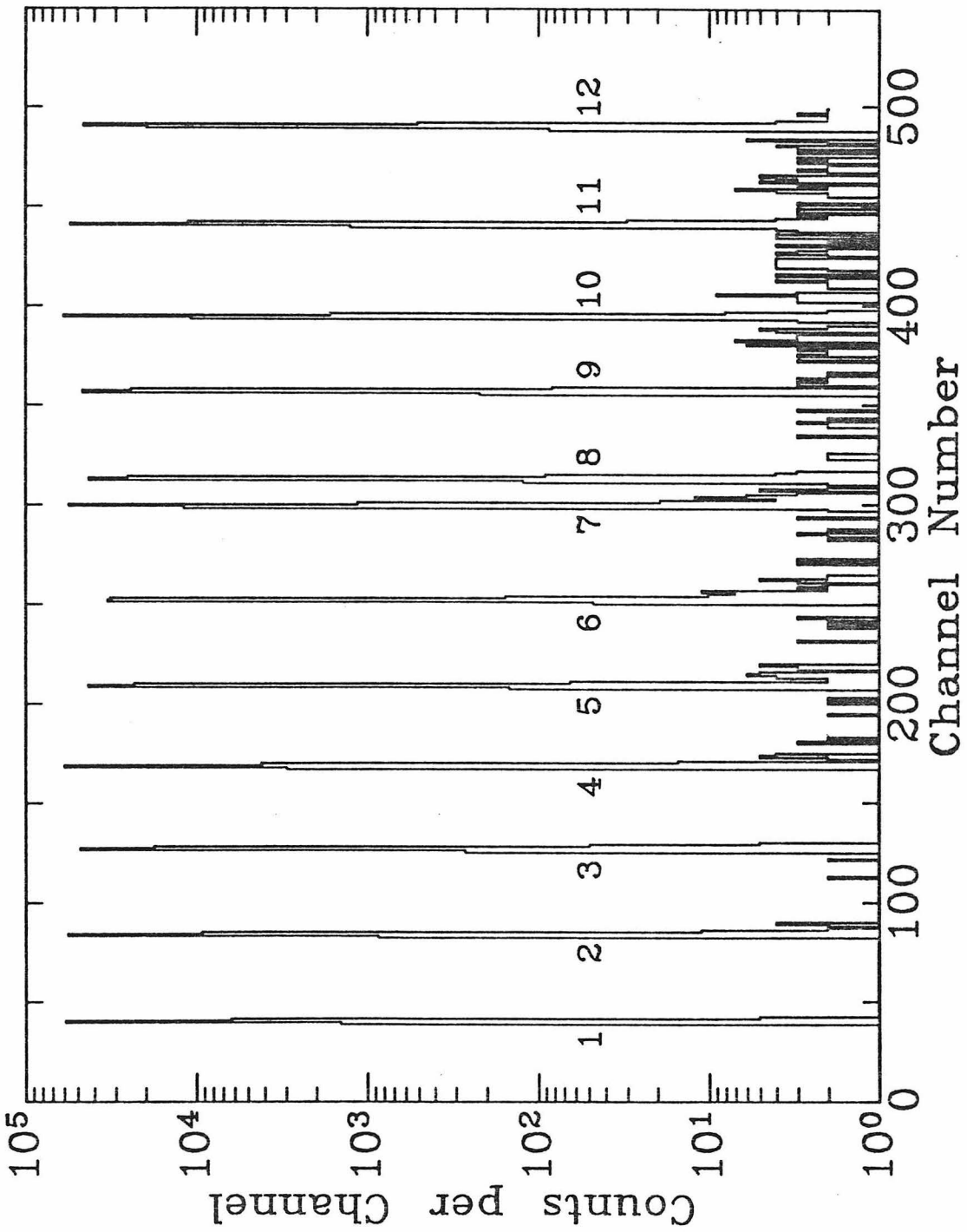
Counts per Channel
10⁵
10⁴
10³
10²
10¹
10⁰
0
100
200
300
400
500
Channel Number
1
2
3
4
5
6
7
8
9
10
11
12

FIGURE 9

Arrangement of the Scintillator for Counting β^+ Particles

The size of the plastic scintillator was just sufficient to stop the highest-energy β^+ particles; this selection minimized background. The entire assembly shown was placed inside the graphite cube in order to count prompt neutrons and delayed β^+ particles within the same bombard-and-count cycle.

FIGURE 9

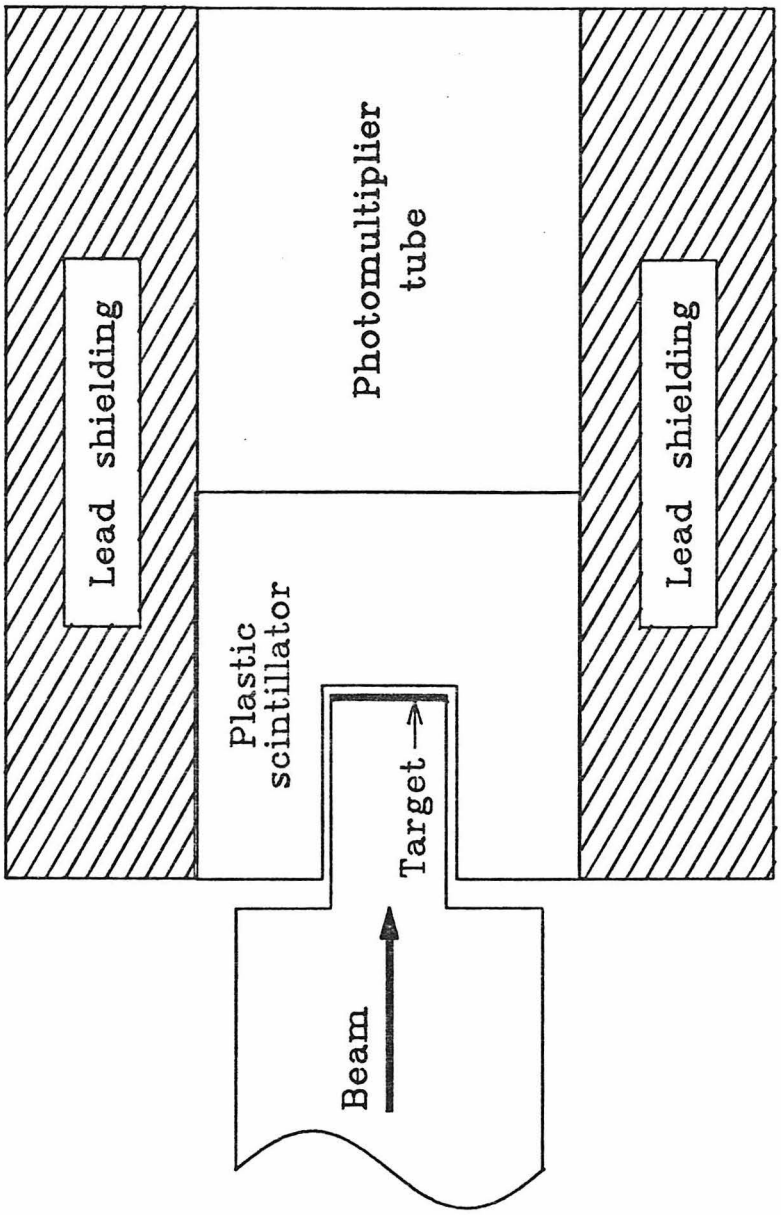
Lead shielding
Photomultiplier tube
Lead shielding
Plastic scintillator
Target
Beam

FIGURE 10

Spectrum from a Ge(Li) Detector Counting a ^{152}Eu Source

All lines marked originate from ^{152}Eu except the one noted; these lines have the following energies and relative intensities (Me78):

Number	Energy (keV)	Intensity	Note
1	244.7	359	
2	344.3	1275	
3	367.8	40.5	
4	411.1	107	
5	444.0	148	
6	778.9	619	
7	964.1	692	
8	1085.9	475	(1)
9	1112.1	649	
10	1408.0	1000	
11	1460.8		(2)
12	1528.1	12.7	

Notes: (1) Includes contributions from unresolved lines at 1084 keV ($I = 11.7$) and 1089.7 keV ($I = 82$).

(2) Background line from ^{40}K

FIGURE 10

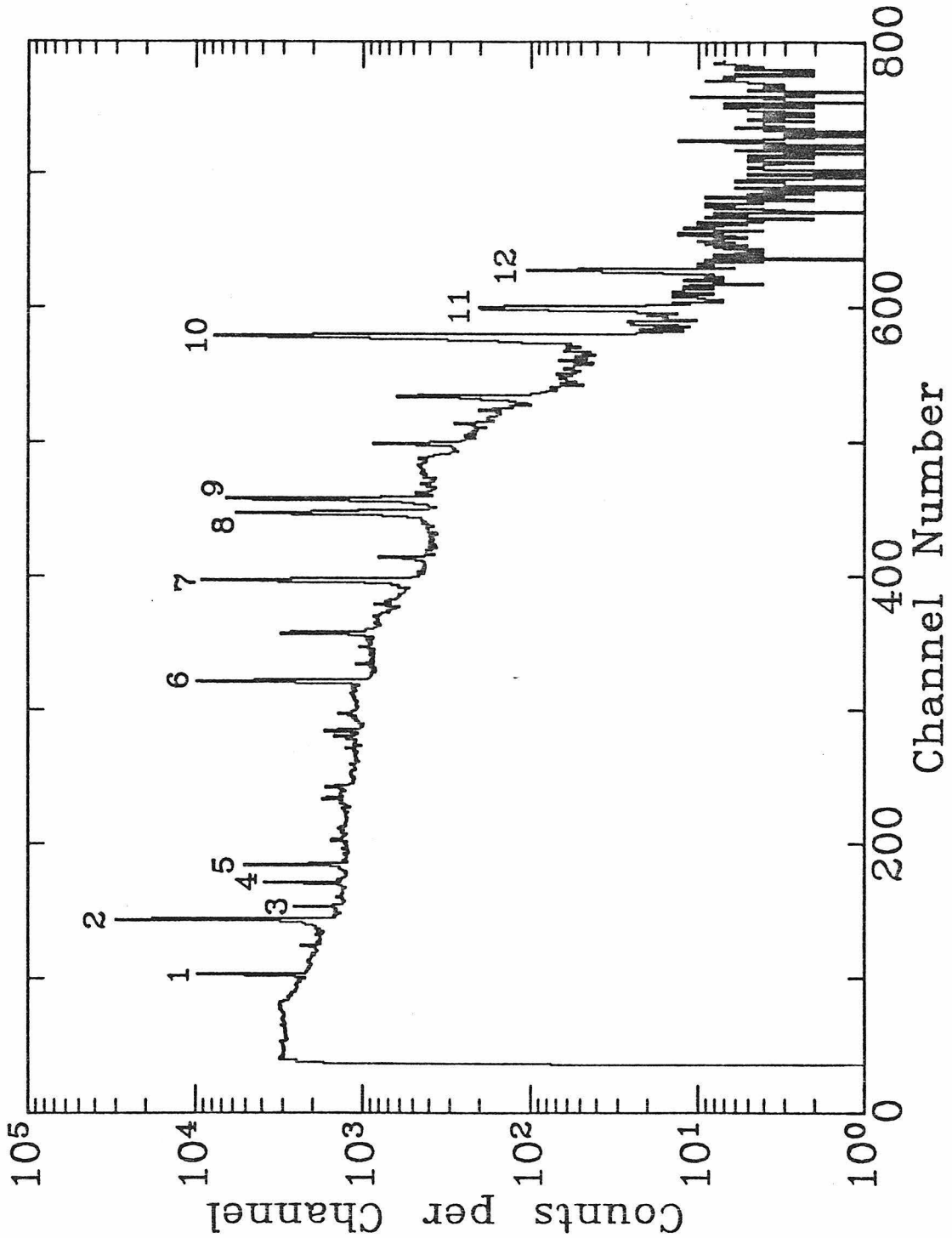
Counts per Channel
Channel Number
10^0
10^1
10^2
10^3
10^4
10^5
0
200
400
600
800
1
2
3
4
5
6
7
8
9
10
11
12

FIGURE 11

Gamma-Ray Detection Efficiency Calibration

The peak efficiency occurs at a relatively high energy because a thin sheet of lead was used to attenuate the lower energy γ-rays. The lead was slightly thicker than would have been ideal, since the linear (power law) portion of the curve does not quite extend to 0.417 MeV; this slightly increases the uncertainty in detection efficiency.

FIGURE 11

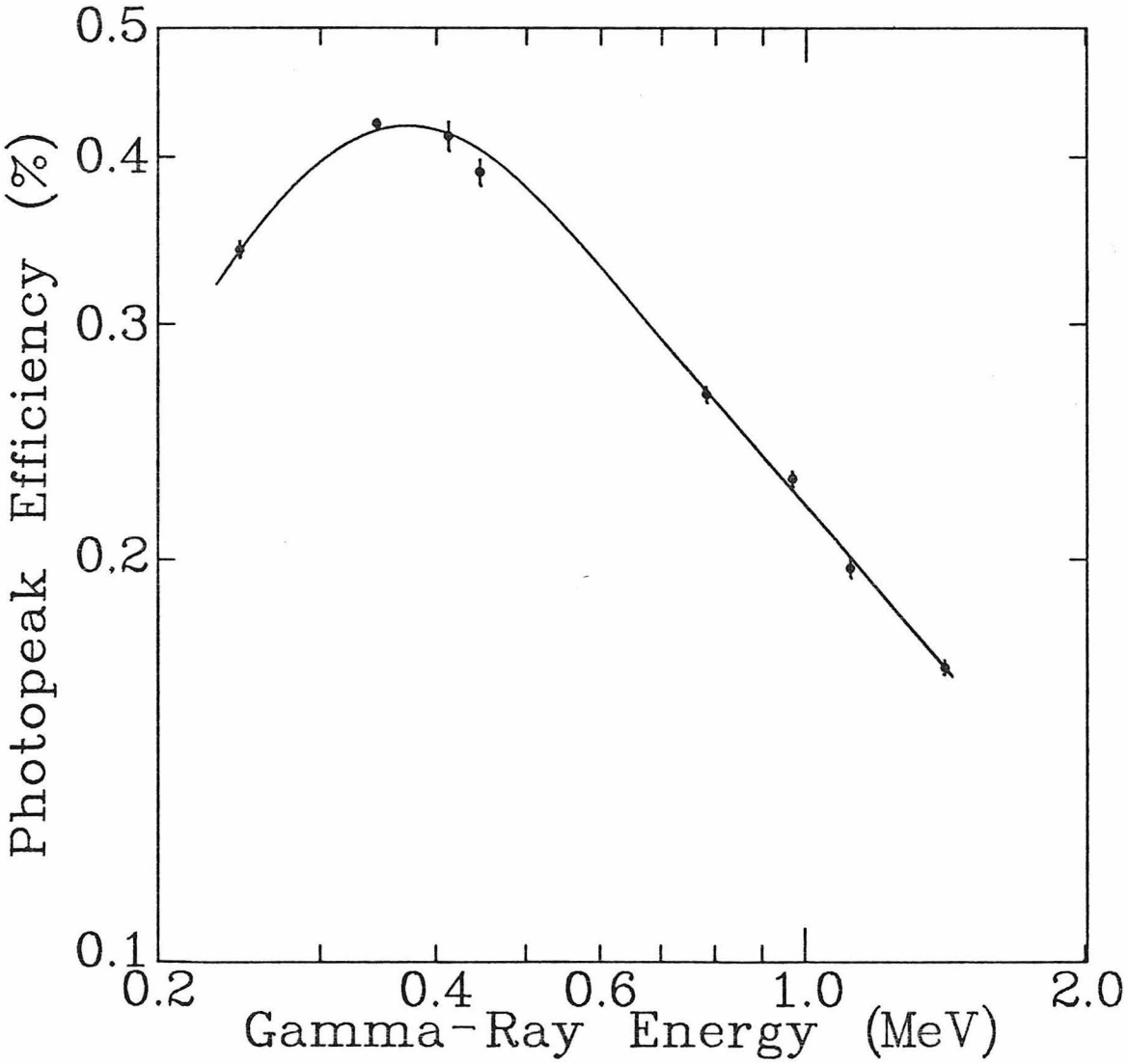
0.5
0.4
0.3
0.2
0.1
Photopeak Efficiency (%)
0.2
0.4
0.6
1.0
2.0
Gamma-Ray Energy (MeV)

FIGURE 12

Typical NaI Spectrum from $^{26}Mg(p,n_1)^{26}Al$ Measurements

The prominent peak (1) is the photopeak from 511-keV annihilation radiation arising from the delayed ^{26m}Al positrons.

FIGURE 12

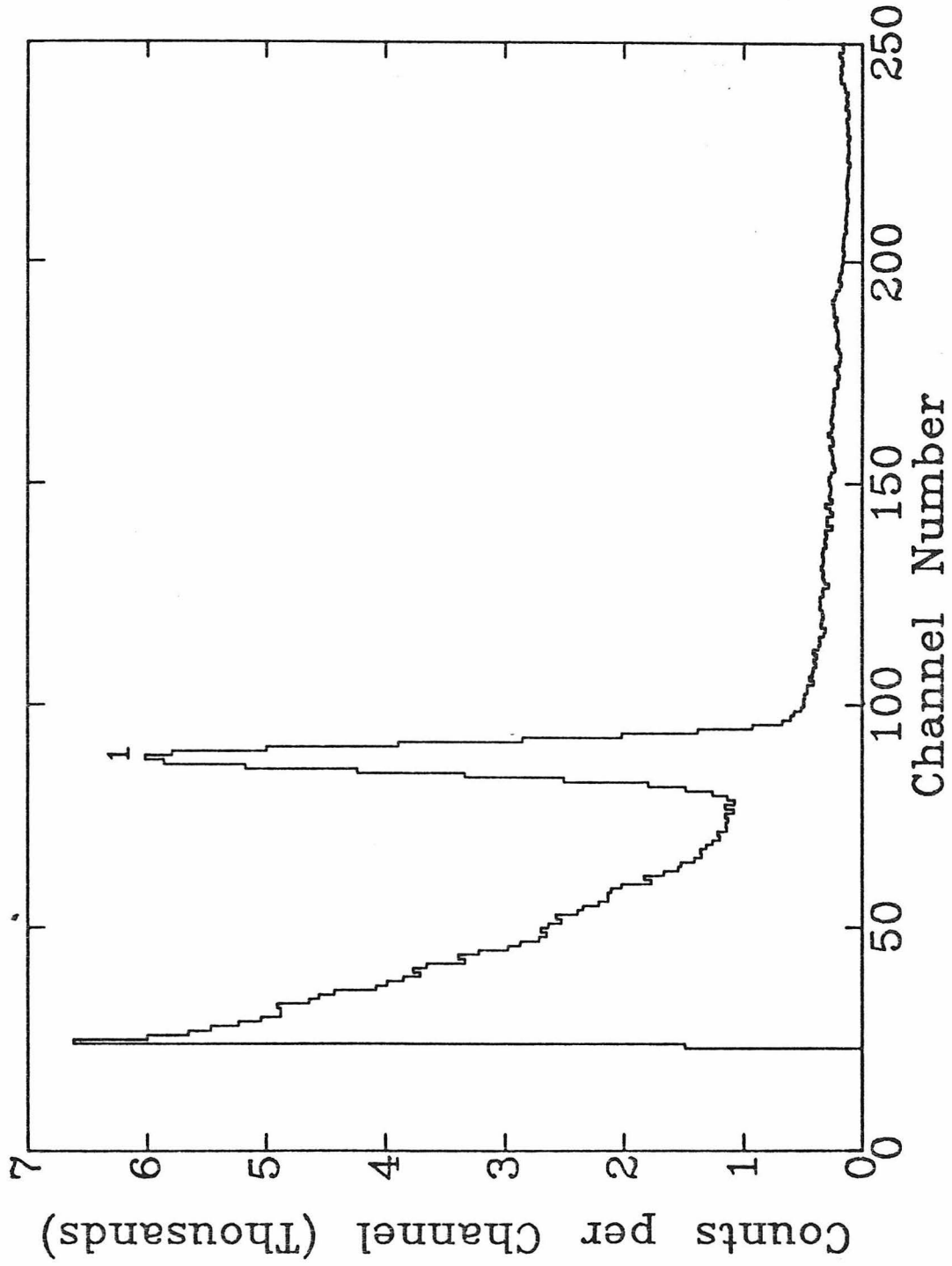
Counts per Channel (Thousands)
0
1
2
3
4
5
6
7
0
50
100
150
200
250
Channel Number
1

FIGURE 13

Times in the Bombard-and-Count Cycle

See equation III.3. The cycle restarts after a time T_T; several cycles (m) are run. Some representative values are as follows:

T_B	T_W	T_C	T_T	m	f_λ
6.25	1.29	9.26	17.00	20	0.470
6.25	1.29	9.26	17.00	40	0.473
5.70	0.30	10.1	16.00	10	0.564

FIGURE 13

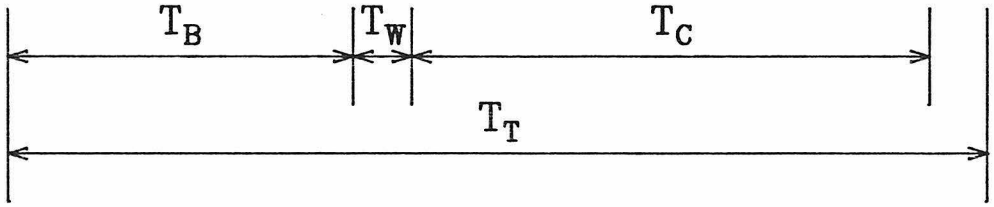

FIGURE 14

Typical Ge(Li) Spectrum from $^{26}Mg(p,n_2)^{26}Al$ Measurements

The target was on a tantalum backing. (Natural tantalum is nearly 100% ^{181}Ta.) The peak of principal interest is that at 417 keV (5). The lines marked are identified as follows:

Number	Energy (keV)	Origin†
1	136	^{181}Ta excitation to 136 keV state
2	165	^{181}Ta excitation to 302 keV state
3	302	^{181}Ta excitation to 302 keV state
4	366	$^{181}Ta(p,n)^{181}W$ to 366-keV state of ^{181}W
5	417	$^{26}Mg(p,n_2)^{26}Al$
6	440	$^{26}Mg(p,\alpha)^{23}Na^*$ to 440-keV state of ^{23}Na
7	511	annihilation radiation; dominant source ^{26m}Al positrons
8	1130	$^{26}Mg(p,p')^{26}Mg^*$ to 2938-keV state of ^{26}Mg
9	1809	$^{26}Mg(p,p')^{26}Mg^*$ to 1089-keV state of ^{26}Mg

† In most cases it is possible that higher excited states than those mentioned are cascading to the state mentioned; this is obviously occurring for (1) and (9) in view the presence of (3) and (8) respectively.

FIGURE 14

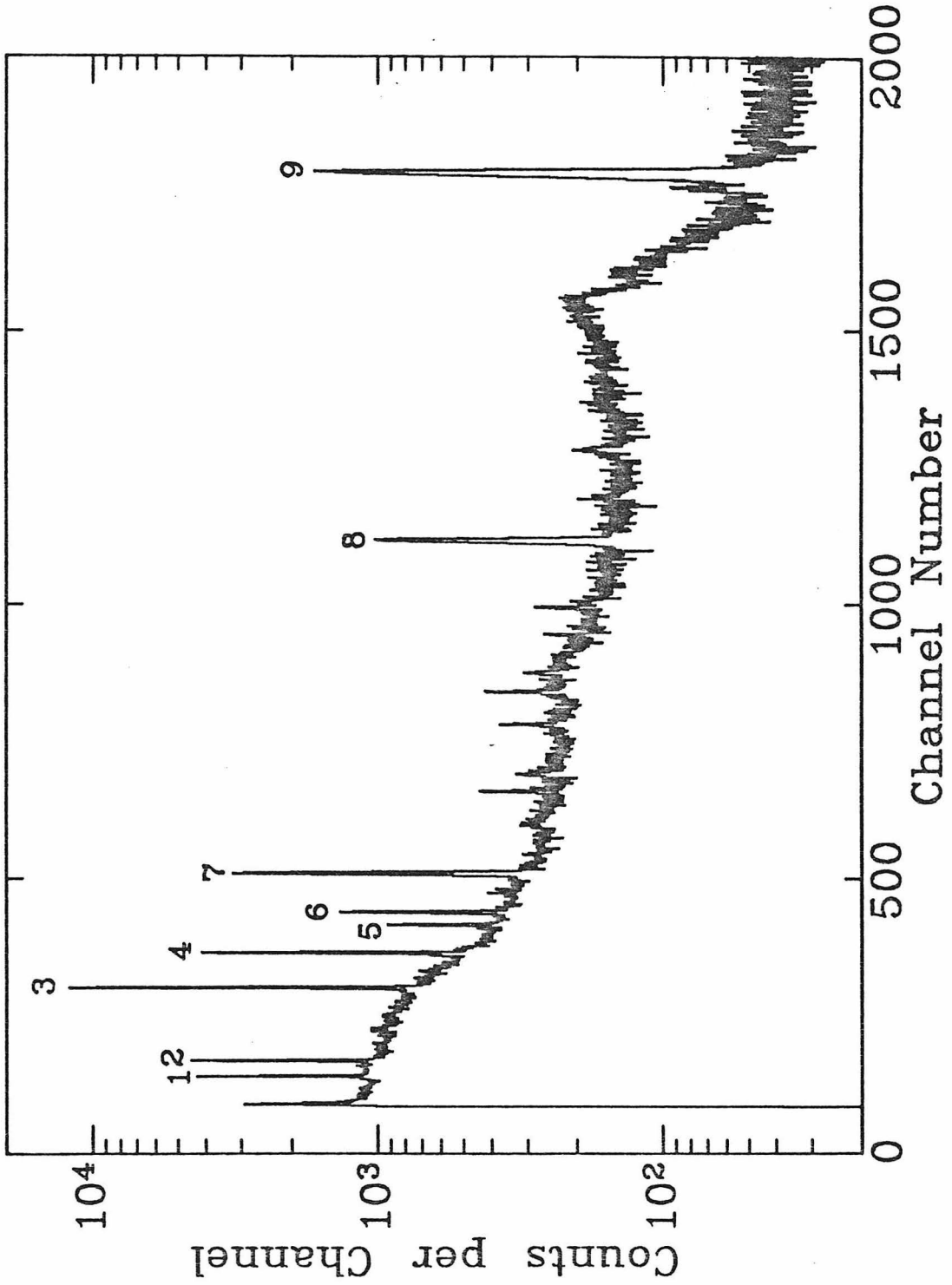
Counts per Channel
10^4
10^3
10^2
0
500
1000
1500
2000
Channel Number
12
3
4
5
6
7
8
9

FIGURE 15

Cross Sections for $^{26}Mg(p,n)^{26}Al$

Excitation functions for (a) $^{26}Mg(p,n_0)^{26}Al$; (b) $^{26}Mg(p,n_1)^{26}Al$; (c) $^{26}Mg(p,n_2)^{26}Al$; (d) the total. In (d) the cross section from threshold to 5.22 MeV is magnified by a factor of 5 to improve visibility.

FIGURE 15

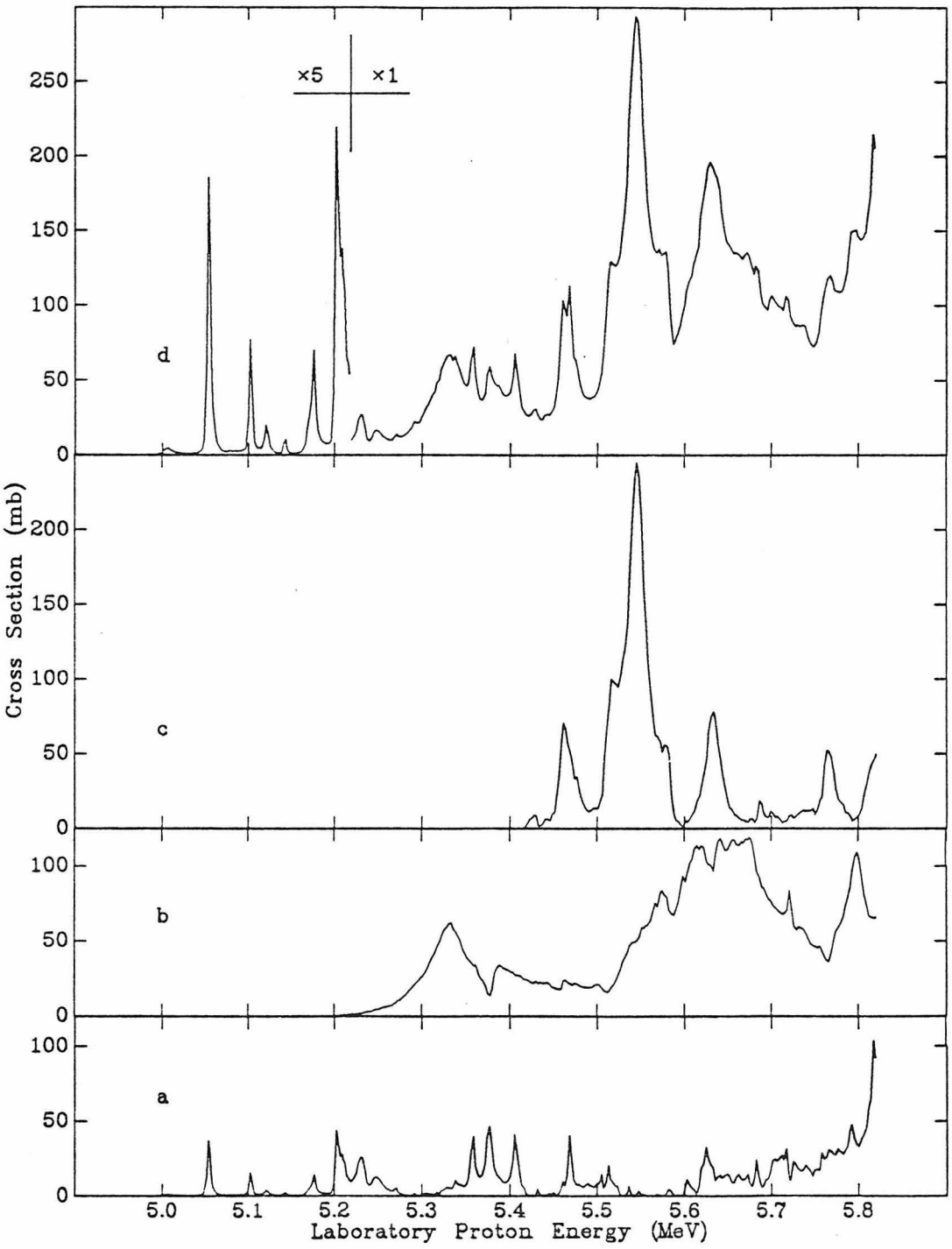
×5
×1
d
c
b
a
Cross Section (mb)
Laboratory Proton Energy (MeV)
0
50
100
150
200
250
5.0
5.1
5.2
5.3
5.4
5.5
5.6
5.7
5.8

FIGURE 16

Cross Sections for $^{23}Na(\alpha,n)^{26}Al$

Experimental excitation functions for (a) $^{23}Na(\alpha,n_0)^{26}Al$; (b) $^{23}Na(\alpha,n_1)^{26}Al$; (c) $^{23}Na(\alpha,n_2)^{26}Al$; and (d) the total. Note that the ordinate scale for (b) is one-tenth that of the others, and note the obviously lower resolution. Generally, it would not be acceptable to have obtained the data of (a) by subtraction from (d) of the low-resolution data of (b); however, since in this case the cross-section values in (b) are such a small fraction of the total, the errors introduced are minimal.

FIGURE 16

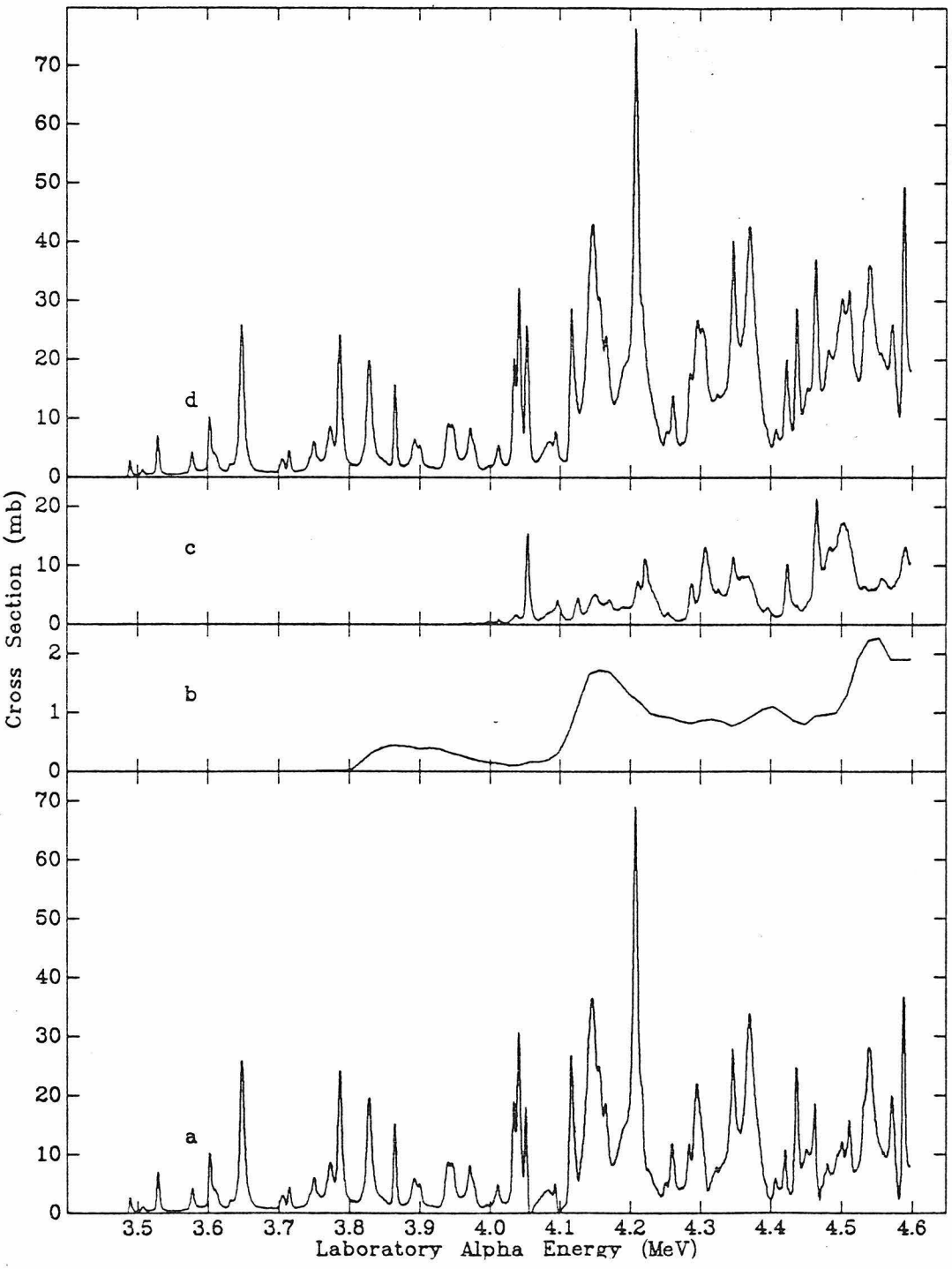
Cross Section (mb)
d
c
b
a
Laboratory Alpha Energy (MeV)
3.5
3.6
3.7
3.8
3.9
4.0
4.1
4.2
4.3
4.4
4.5
4.6

FIGURE 17

Comparison to Previous $^{26}Mg(p,n)^{26}Al$ (0) Measurements

Comparison of data from the present experiment (solid line) to data from Paul *et al.* (Pa80) (open circles) and to Furukawa *et al.* (Fu71) (solid circle). The data shown represent the total production of ^{26}Al in the ground state, either directly or via γ-ray emission from a higher state, in the $^{26}Mg(p,n)^{26}Al$ reaction.

FIGURE 17

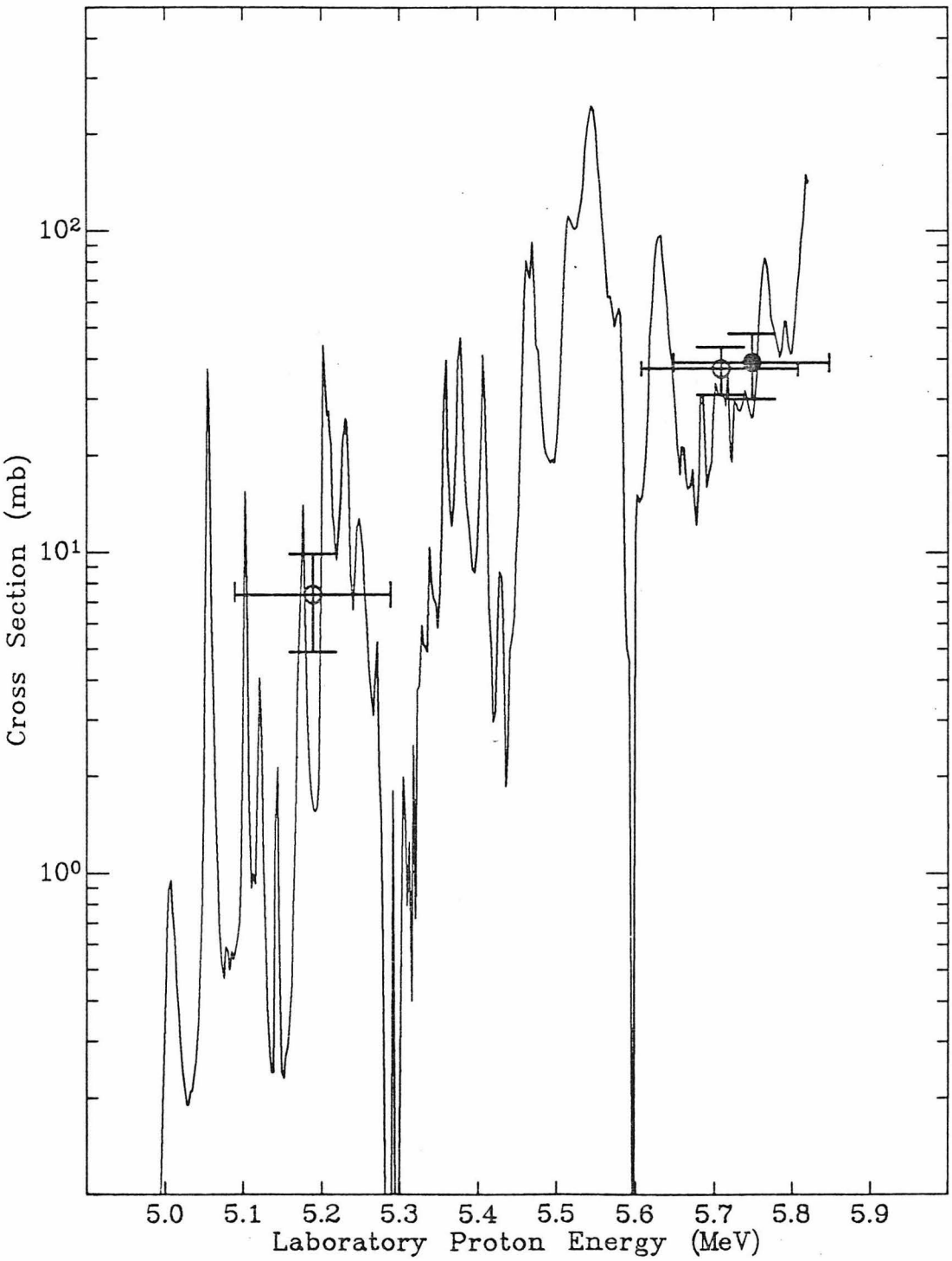
Cross Section (mb)
10^2
10^1
10^0
5.0
5.1
5.2
5.3
5.4
5.5
5.6
5.7
5.8
5.9
Laboratory Proton Energy (MeV)

FIGURE 18

Comparison to Previous $^{26}Mg(p,n_1)^{26}Al$ Measurement

Comparison of data from the present experiment (solid line) to that of King and Cheng (Ki79) (open circles) for the $^{26}Mg(p,n_1)^{26}Al$ reaction, determined by measuring delayed β^+ activity. The discrepancies are well outside of the estimated uncertainties for all except the point at 5.75 MeV.

FIGURE 18

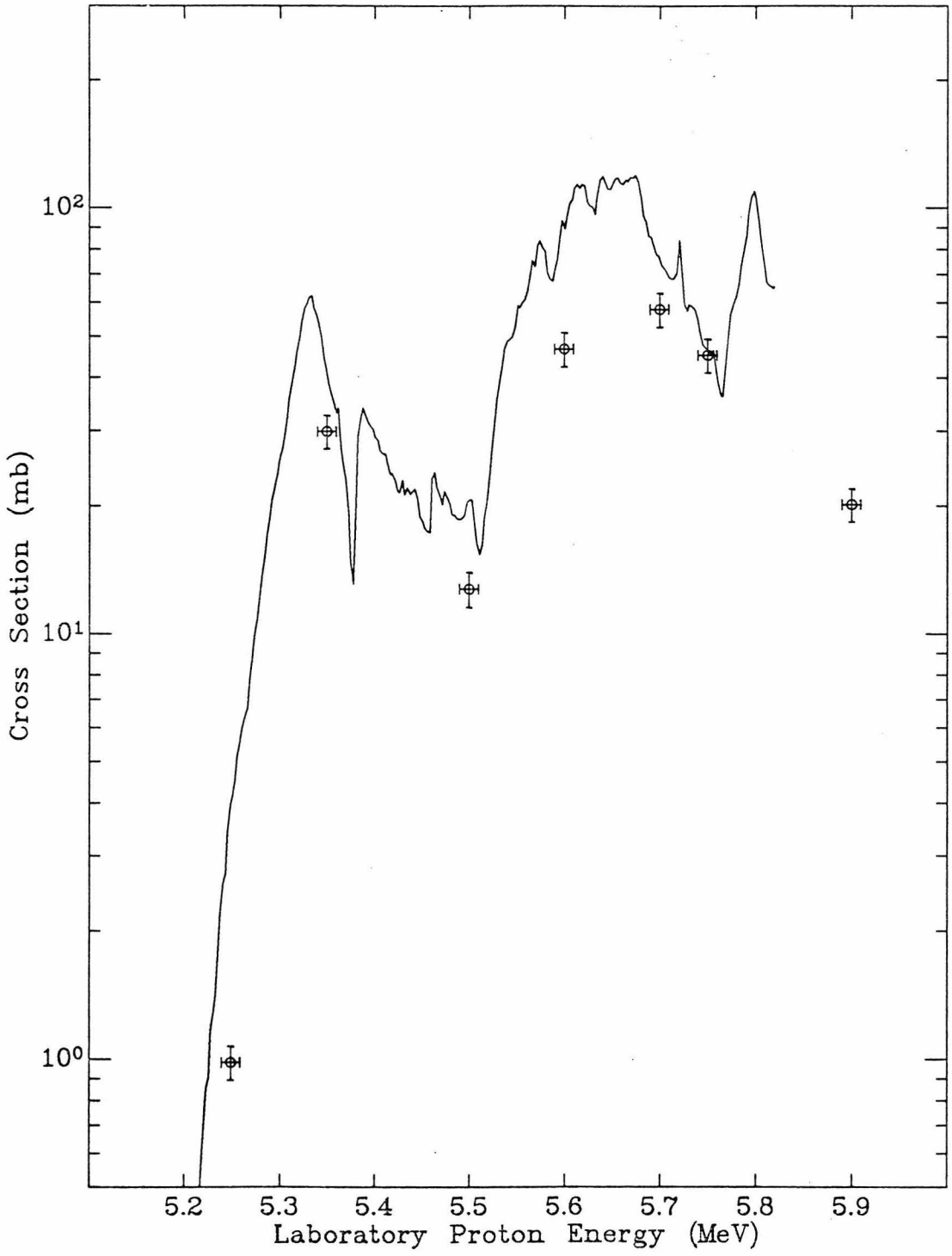
Cross Section (mb)
10^2
10^1
10^0
5.2
5.3
5.4
5.5
5.6
5.7
5.8
5.9
Laboratory Proton Energy (MeV)

FIGURE 19

Comparison to Previous $^{26}Mg(p,n_2)^{26}Al$ Measurement

Comparison of data from the present experiment (solid line) to the data of Norman *et al.* (No81a) (open circles) for yield to the 417-keV state.

FIGURE 19

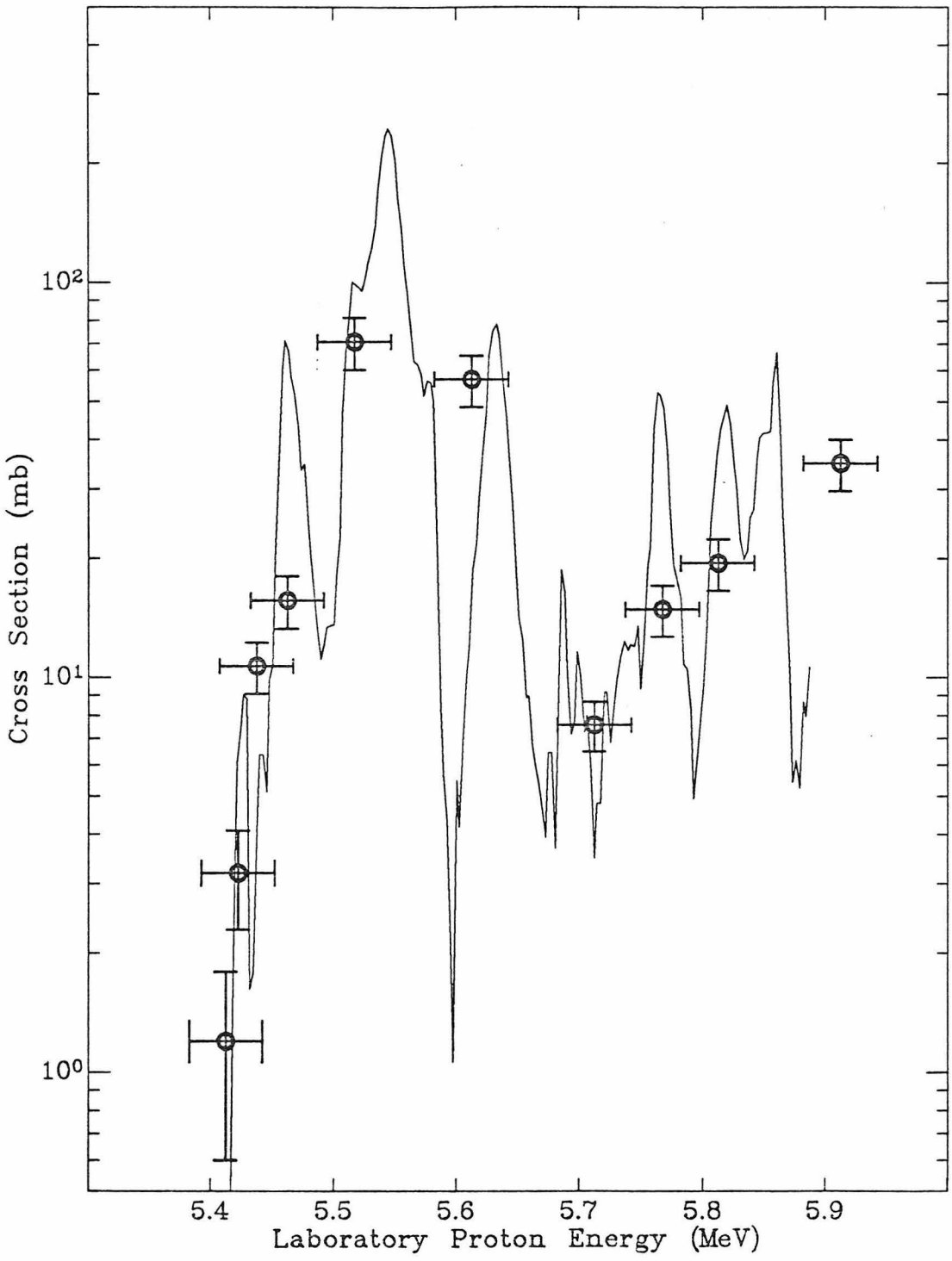
Cross Section (mb)
10²
10¹
10⁰
5.4
5.5
5.6
5.7
5.8
5.9
Laboratory Proton Energy (MeV)

FIGURE 20

Comparison to Previous $^{26}Mg(p,n)^{26}Al$ Measurement

Comparison of data from the present experiment (solid line) to the data of Norman *et al.* (No81b) (open circles) for total neutron yield in the $^{26}Mg(p,n)^{26}Al$ reaction. The results of the previous experiment were obtained by differentiating the yield from a thick target.

FIGURE 20

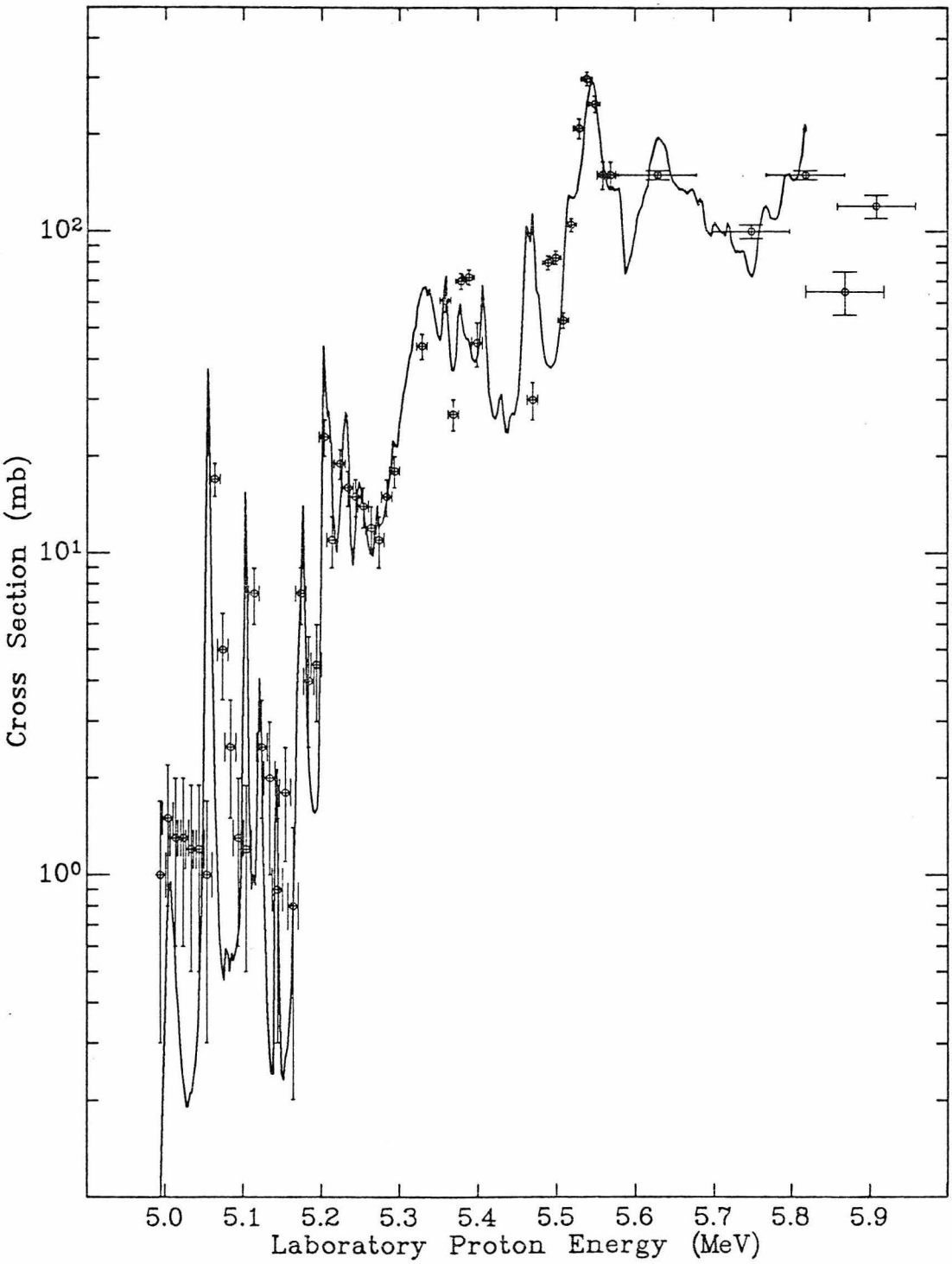
Cross Section (mb)
10²
10¹
10⁰
5.0
5.1
5.2
5.3
5.4
5.5
5.6
5.7
5.8
5.9
Laboratory Proton Energy (MeV)

FIGURE 21

Comparison to Previous $^{23}Na(\alpha,n)^{26}Al$ Measurement

Comparison of data from the present experiment (solid line) to the data of Norman *et al.* (No82) (circles) for the total neutron yield in the $^{23}Na(\alpha,n)^{26}Al$ reaction. The results of the previous experiment were obtained by differentiating the yield from a thick target.

FIGURE 21

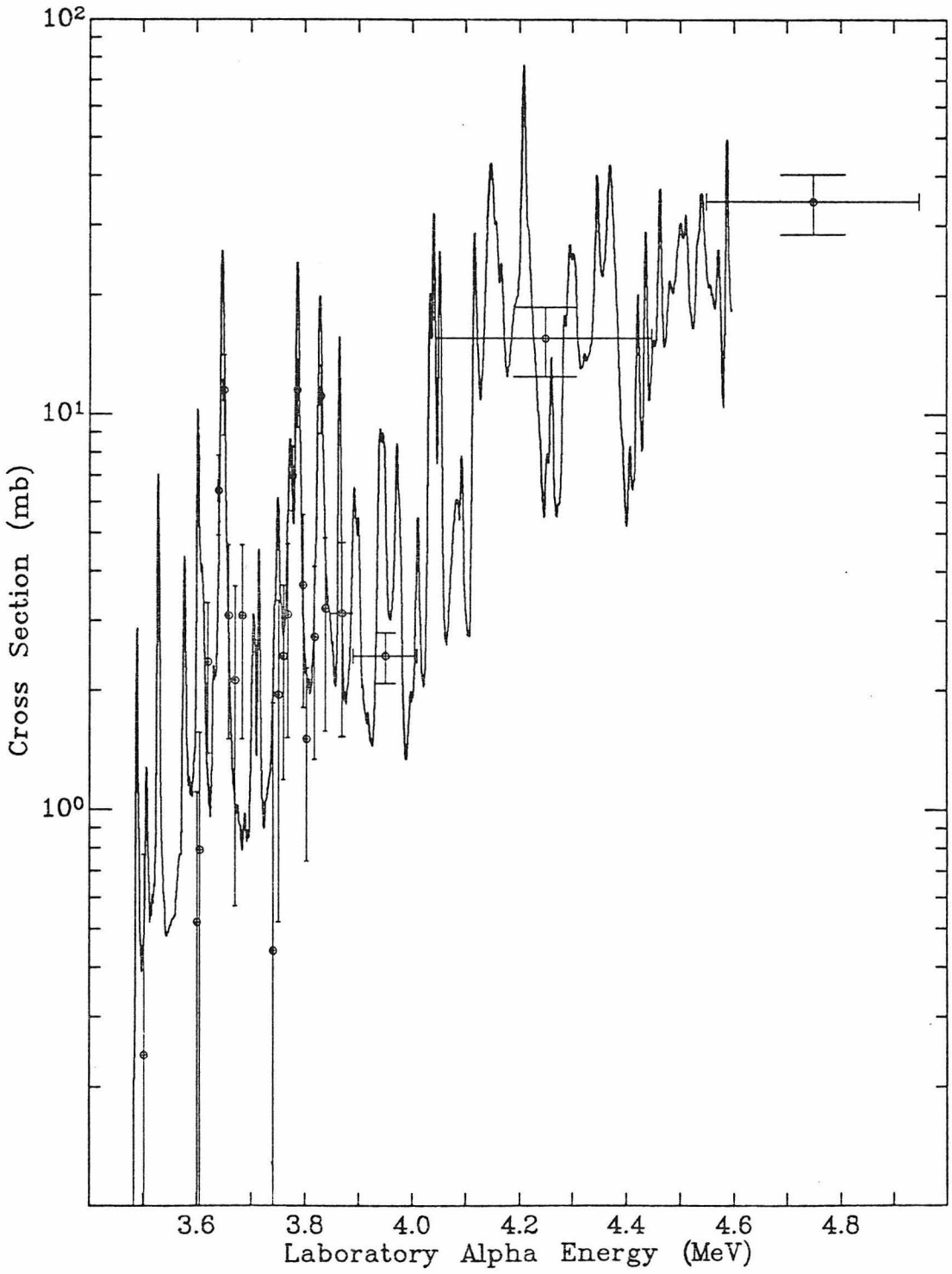
10^2
10^1
10^0
Cross Section (mb)
3.6
3.8
4.0
4.2
4.4
4.6
4.8
Laboratory Alpha Energy (MeV)

FIGURE 22

Comparison to Previous $^{23}Na(\alpha,n_1)^{26}Al$ Measurement

Comparison of data from the present experiment (solid line) to the data of Norman *et al.* (No82) (open circles) for the $^{23}Na(\alpha,n_1)^{26}Al$ reaction, determined by measuring the delayed positron yield.

FIGURE 22

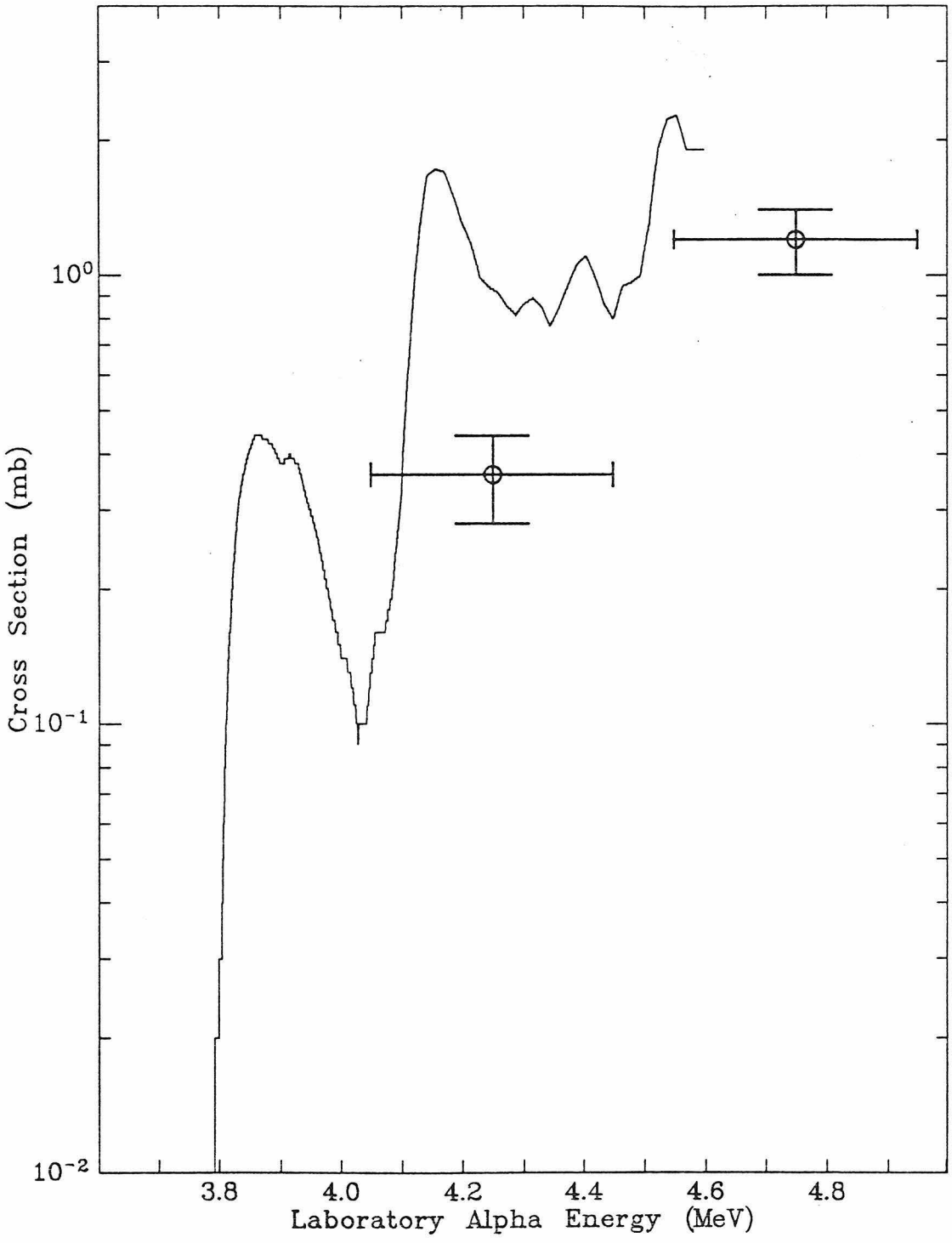
Cross Section (mb)
10^0
10^{-1}
10^{-2}
3.8
4.0
4.2
4.4
4.6
4.8
Laboratory Alpha Energy (MeV)

FIGURE 23

Comparison to Previous $^{23}Na(\alpha,n_2)^{26}Al$ Measurement

Comparison of data from present experiment (solid line) to the data of Norman *et al.* (No82) (open circles) for the $^{23}Na(\alpha,n_2)^{26}Al$ reaction, determined by measuring the 417-keV γ-ray yield.

FIGURE 23

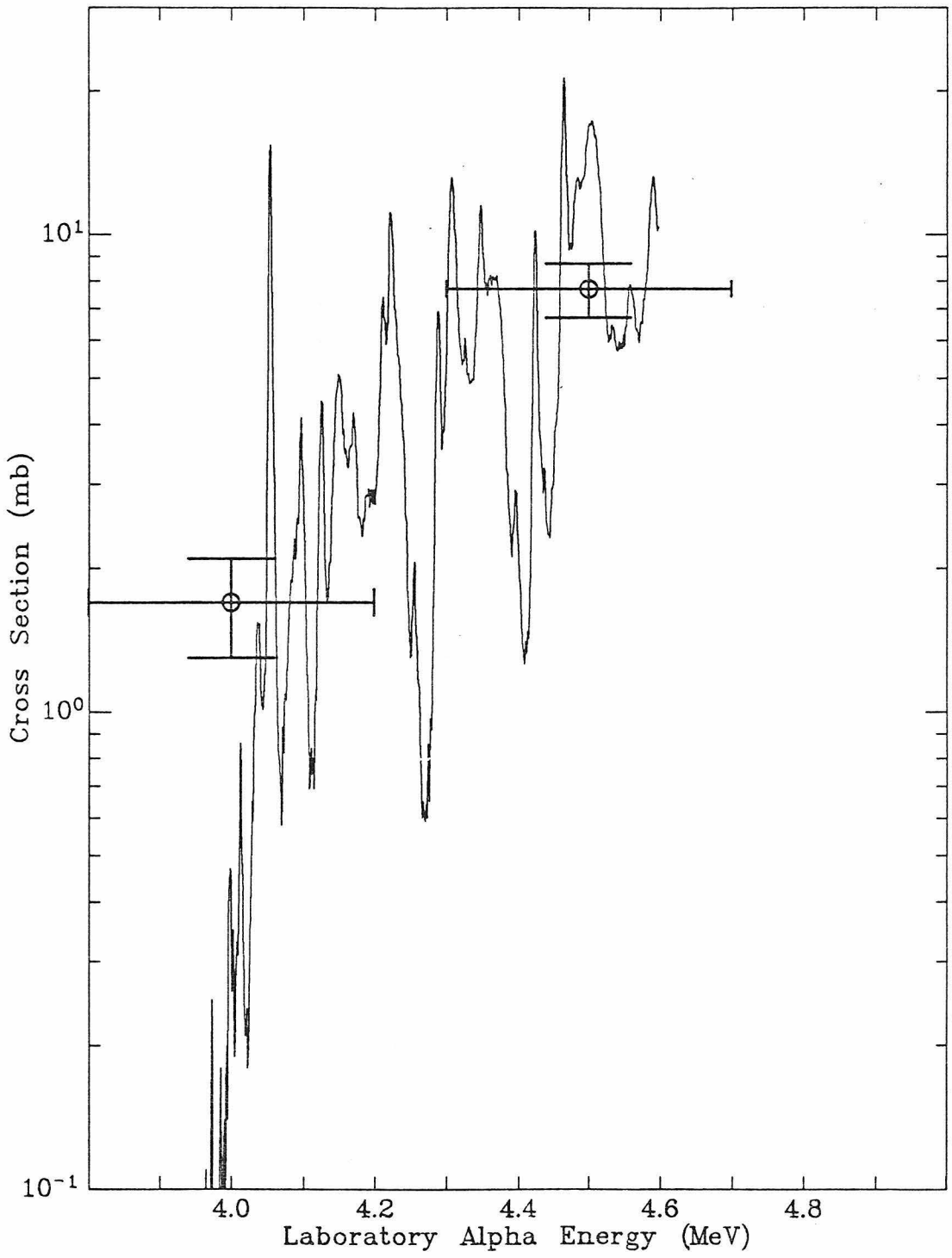
Cross Section (mb)
10^1
10^0
10^{-1}
4.0
4.2
4.4
4.6
4.8
Laboratory Alpha Energy (MeV)

FIGURE 24

$^{26}Al(n_i,p)^{26}Mg$ Cross Sections

Experimental excitation functions (solid) for (a) $^{26}Al(n_0,p)^{26}Mg$; (b) $^{26}Al(n_1,p)^{26}Mg$; and (c) $^{26}Al(n_2,p)^{26}Mg$. These were calculated by the principle of detailed balance from the data of figures 15(a), (b), and (c) respectively. The results of a Hauser-Feshbach optical model calculation (dashed) are also shown. Note that the ordinate scale for (a) is one-tenth that of (b) and (c). The substantial theoretical overestimation of the $^{26}Al(n_0,p)^{26}Mg$ cross section is apparent, as is the tendency of the theory to overestimate all cross sections at low energy.

FIGURE 24

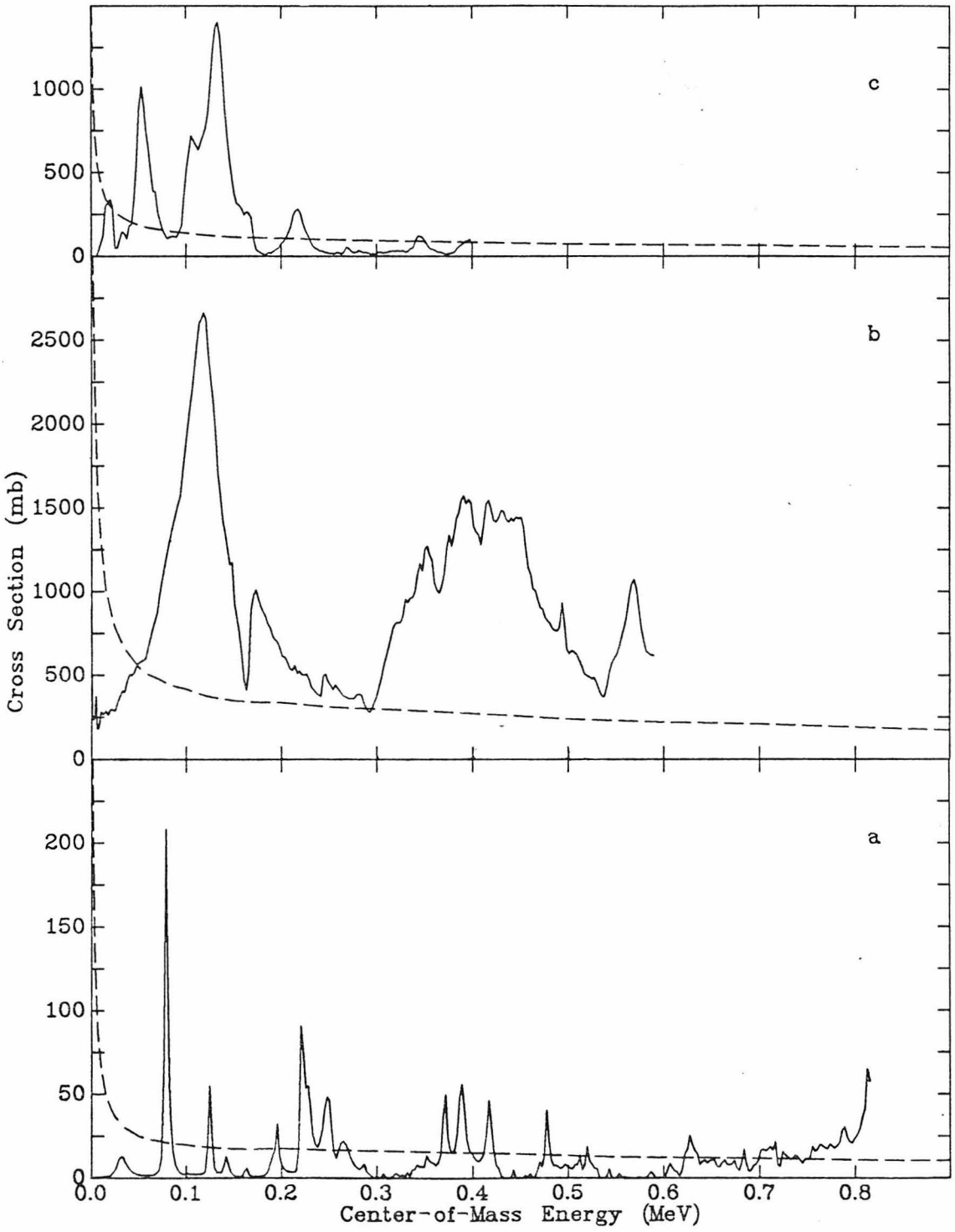
c
b
a
Cross Section (mb)
Center-of-Mass Energy (MeV)
0
500
1000
1500
2000
2500
50
100
150
200
0.0
0.1
0.2
0.3
0.4
0.5
0.6
0.7
0.8

FIGURE 25

$^{26}Al(n_i,\alpha)^{23}Na$ Cross Sections

Experimental excitation functions (solid) for (a) $^{26}Al(n_0,\alpha)^{23}Na$; (b) $^{26}Al(n_1,\alpha)^{23}Na$; and (c) $^{26}Al(n_2,\alpha)^{23}Na$. These were calculated by the principle of detailed balance from the data of figures 16(a), (b), and (c) respectively. The fine dashed lines in (a) and (c) are the results of the present experiment reduced by a factor of 5 to fit on the plot. The results of a Hauser-Feshbach optical model calculation (coarse dashed) are also shown. The "kinks" in the dashed curve are strictly an artifact introduced by the fact that the computation was carried out over a rather coarse grid of bombardment energies. The substantial overestimation of $^{26}Al(n_2,\alpha)^{23}Na$ and underestimation of $^{26}Al(n_0,\alpha)^{23}Na$ are apparent.

FIGURE 25

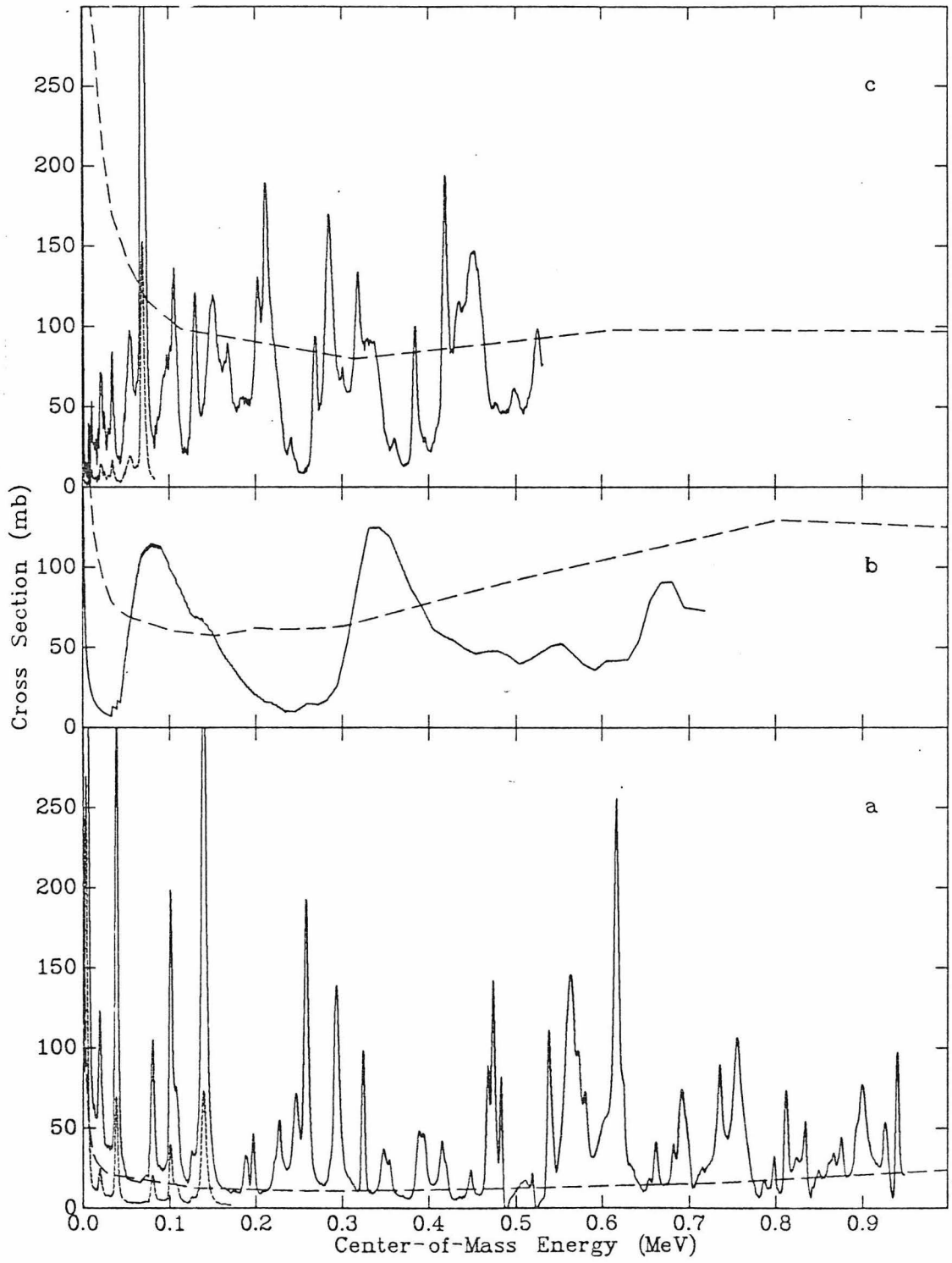
c
b
a
Cross Section (mb)
Center-of-Mass Energy (MeV)
0
50
100
150
200
250
0.0
0.1
0.2
0.3
0.4
0.5
0.6
0.7
0.8
0.9

FIGURE 26

Ratios of Reaction Rates for $^{26}Al(n_i,p)^{26}Mg$

Ratios of reaction rates calculated from the theoretical cross-section values of the Hauser-Feshbach calculation (figure 15) to the reaction rates calculated from the cross-section data of the present experiment for (a) $^{26}Al(n_0,p)^{26}Mg$; (b) $^{26}Al(n_1,p)^{26}Mg$; and (c) $^{26}Al(n_2,p)^{26}Mg$ *vs* temperature. In each case, the reactions are to the ground state of ^{26}Mg.

FIGURE 26

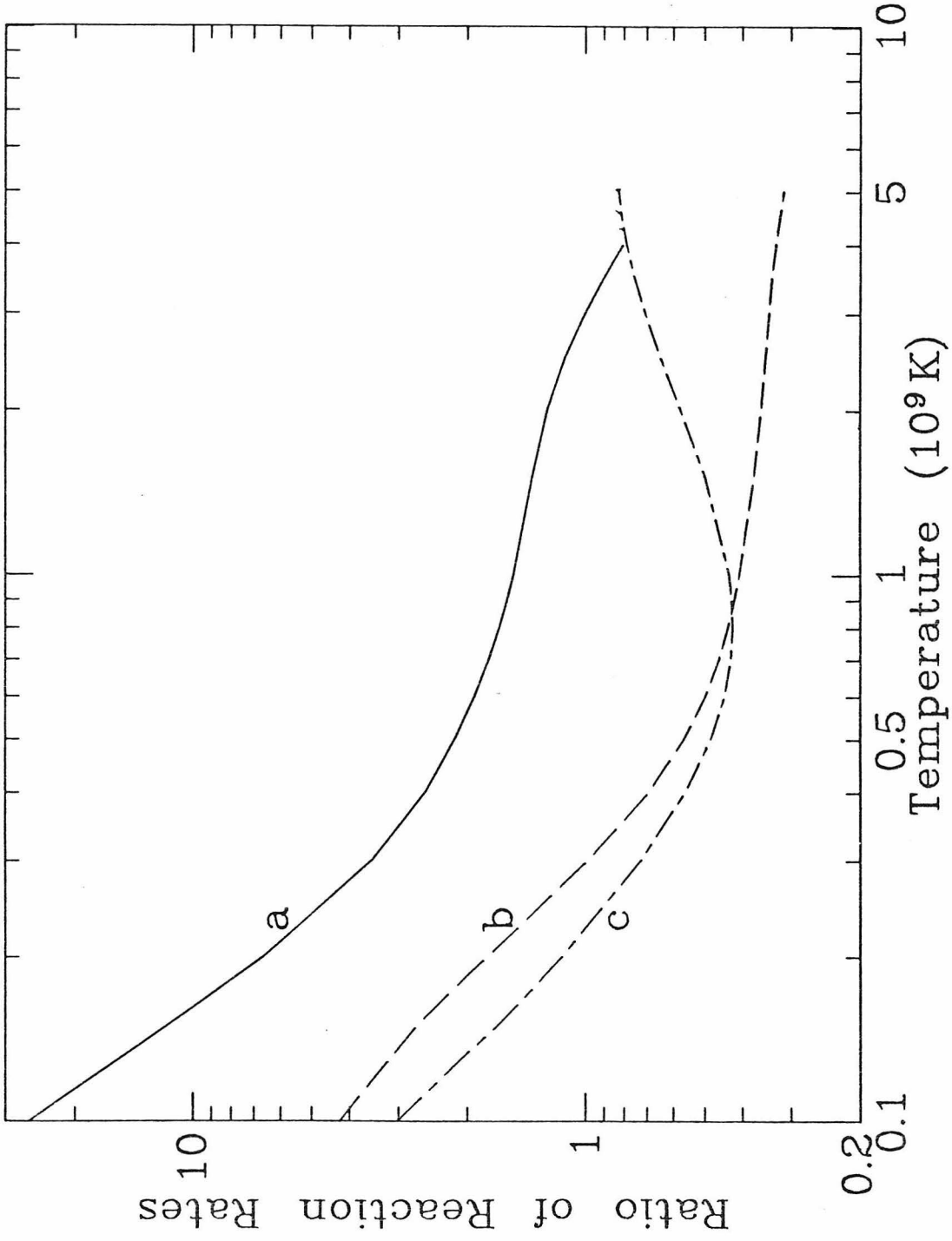
Ratio of Reaction Rates
10
1
0.2
0.1
0.5
1
5
10
Temperature (10⁹ K)
a
b
c

FIGURE 27

Ratios of Reaction Rates for $^{26}Al(n_i, \alpha)^{23}Na$

Ratios of reaction rates calculated from theoretical cross-section values of the Hauser-Feshbach calculation (figure 16) to the reaction rates calculated from the cross section data of the present experiment for (a) $^{26}Al(n_0, \alpha)^{23}Na$; (b) $^{26}Al(n_1, \alpha)^{23}Na$; and (c) $^{26}Al(n_2, \alpha)^{23}Na$ *vs* temperature. In each case, the reactions are to the ground state of ^{23}Na.

FIGURE 27

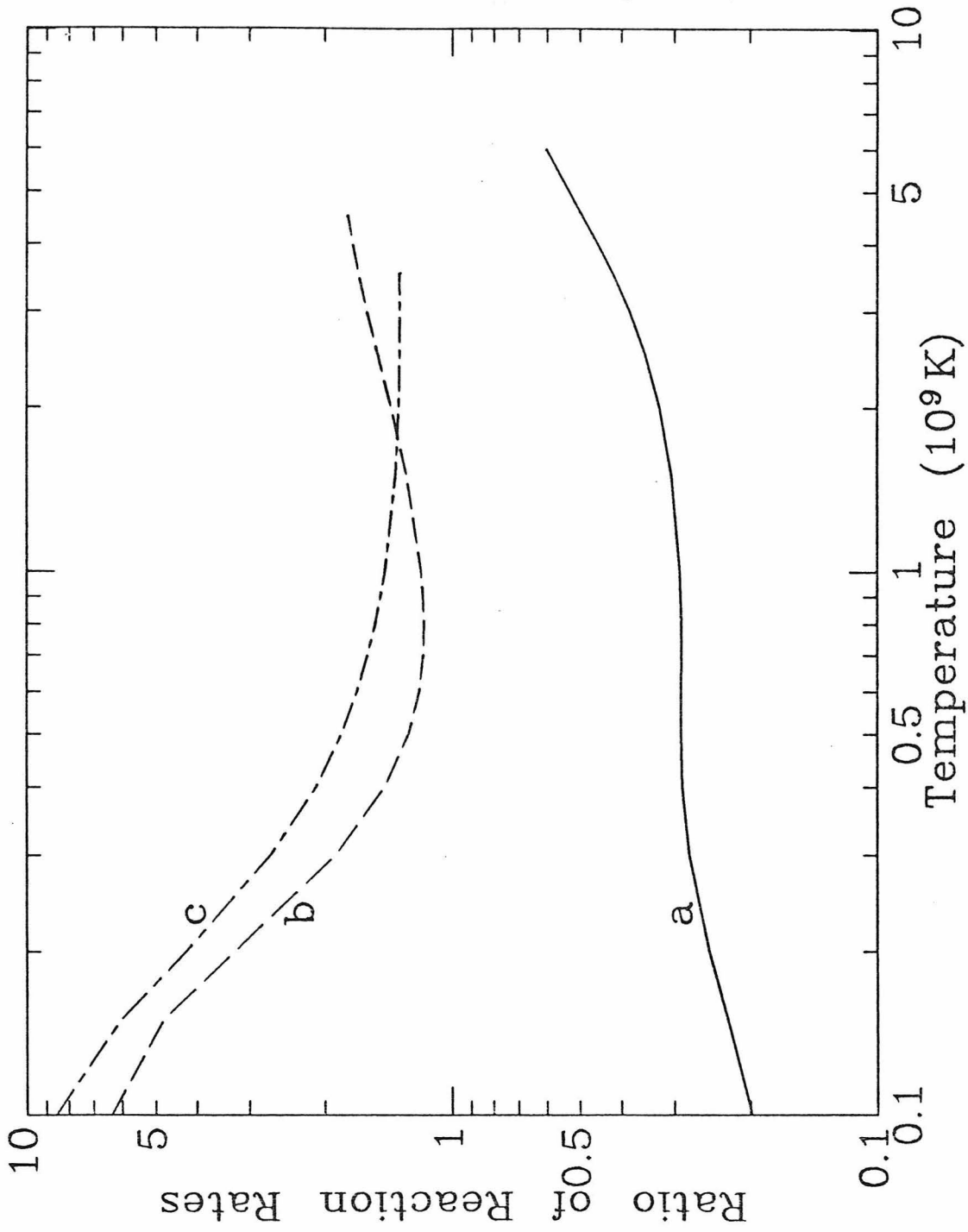
Ratio of Reaction Rates
10
5
1
0.5
0.1
0.1
0.5
1
5
10
Temperature (10⁹K)
a
b
c

FIGURE 28

Reaction Rate Factors

Reaction rate factors for (a) $^{26}Al(n_0,p_0)^{26}Mg$ (calculated from the data of the present experiment); (b) $^{26}Al(n_0,\alpha_0)^{23}Na$ (calculated from the data of the present experiment); (c) $^{26}Al(n_0,p_t)^{26}Mg$ (as tabulated by Caughlan *et al.*) (Ca84); and (d) $^{26}Al(n_0,\alpha_t)^{23}Na$ (Ca84). The values represented by (c) are expected to be dominated by reactions to the excited states of ^{26}Mg; therefore it is not surprising that (c) should be so much higher than (a). What is surprising is that (b) should be higher than (d); the theory apparently underestimates significantly the $^{26}Al(n_0,\alpha_0)^{23}Na$ reaction rate.

FIGURE 28

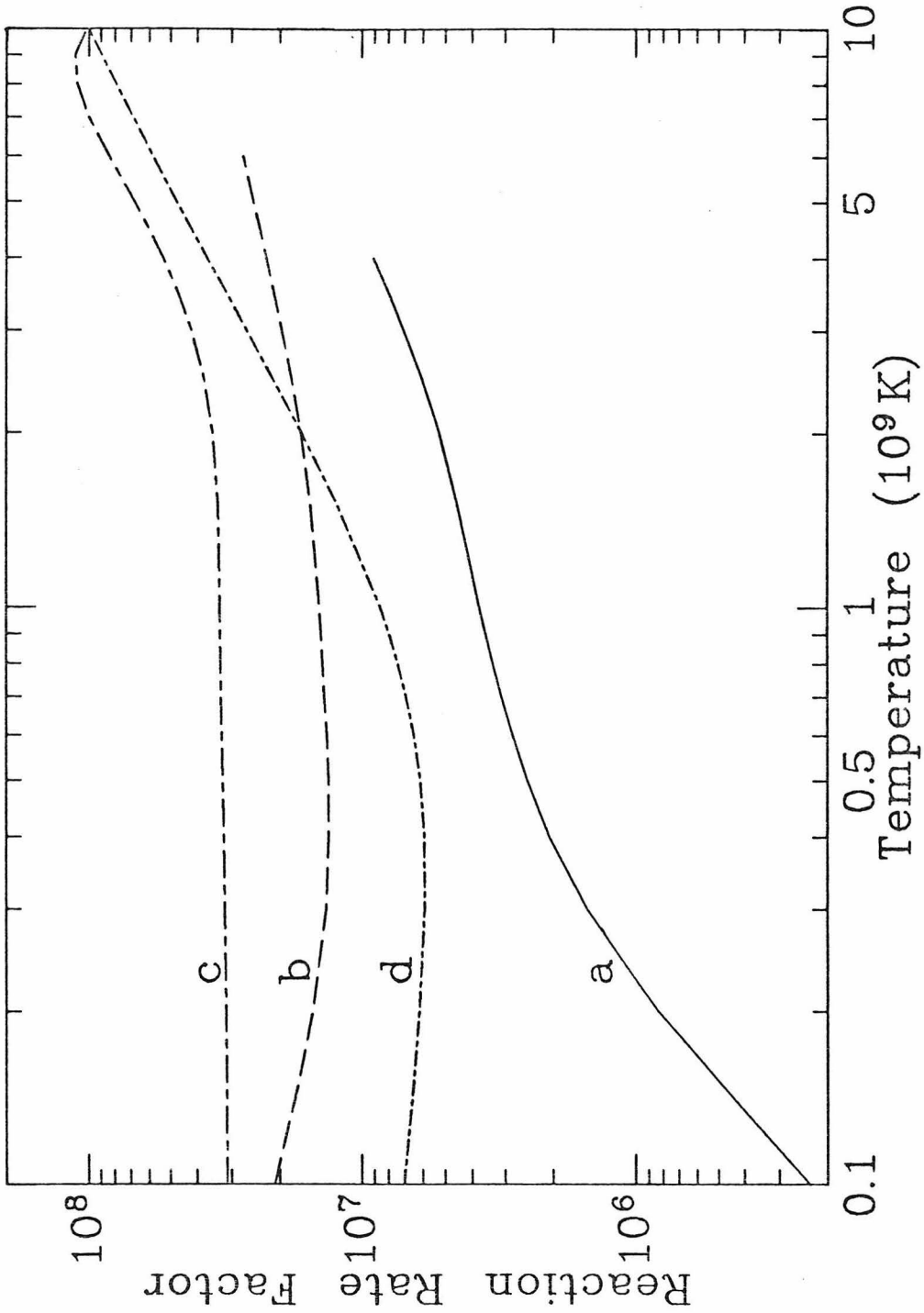
Reaction Rate Factor
10^8
10^7
10^6
0.1
0.5
1
5
10
Temperature (10^9K)
a
b
c
d

FIGURE 29

Excitation Functions for $^{26}Mg(p,n)^{26}Al$

These are the same data as presented in figure 15, except that here they are plotted *vs* excitation energy in the compound nucleus (^{27}Al) to facilitate comparison with other excitation functions presented in figures 29 through 32.

FIGURE 29

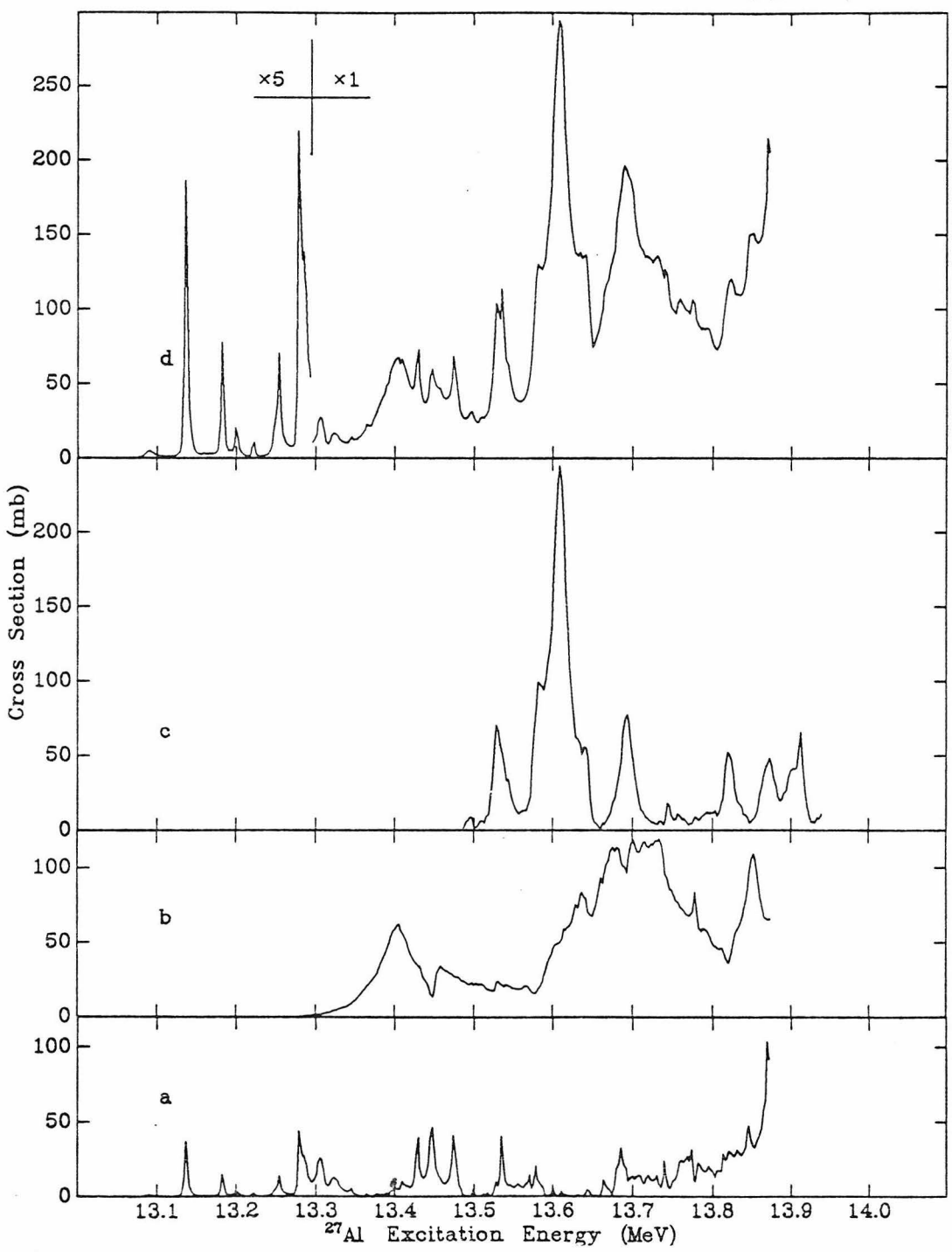
×5
×1
d
c
b
a
Cross Section (mb)
250
200
150
100
50
0
13.1
13.2
13.3
13.4
13.5
13.6
13.7
13.8
13.9
14.0
^{27}Al Excitation Energy (MeV)

FIGURE 30

Excitation Functions for $^{23}Na(\alpha,n)^{26}Al$

These are the same data as presented in figure 16, except that here they are plotted *vs* excitation energy in the compound nucleus (^{27}Al) to facilitate comparison with other excitation functions presented in figures 29 through 32.

FIGURE 30

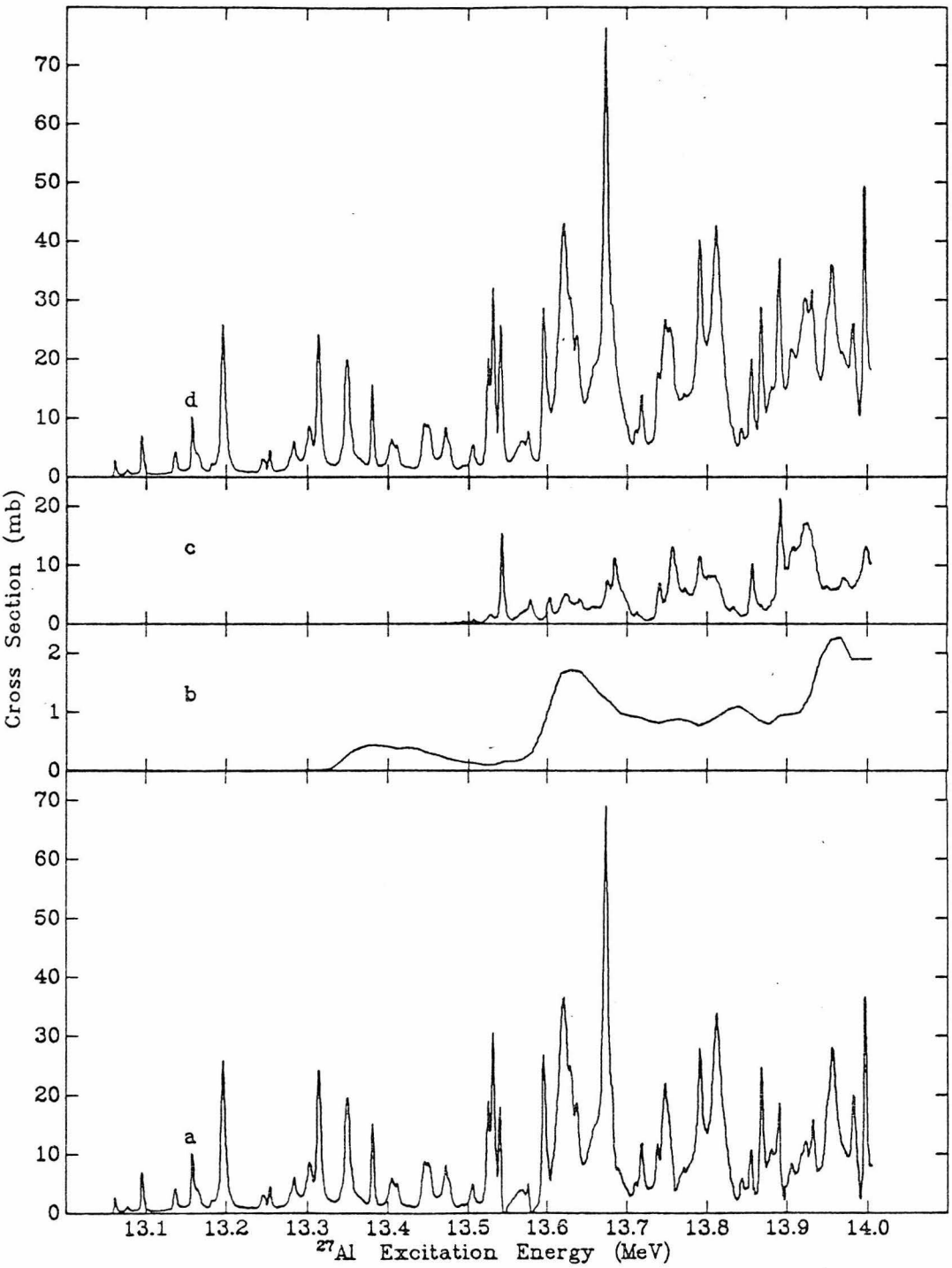
Cross Section (mb)
d
c
b
a
70
60
50
40
30
20
10
0
2
1
13.1
13.2
13.3
13.4
13.5
13.6
13.7
13.8
13.9
14.0
27Al Excitation Energy (MeV)

FIGURE 31

Excitation functions for $^{26}Mg(p,p')^{26}Mg^{*}$

Excitation functions for $^{26}Mg(p,p')^{26}Mg^{*}$ leading to (a) the 1809-keV γ-ray; (b) the 1130-keV γ-ray; (c) the 1780-keV γ-ray; and (d) the 1004-keV γ-ray. Note the reduced scale for the last two, which represent respectively excitations to the third and fourth excited states of ^{26}Mg.

FIGURE 31

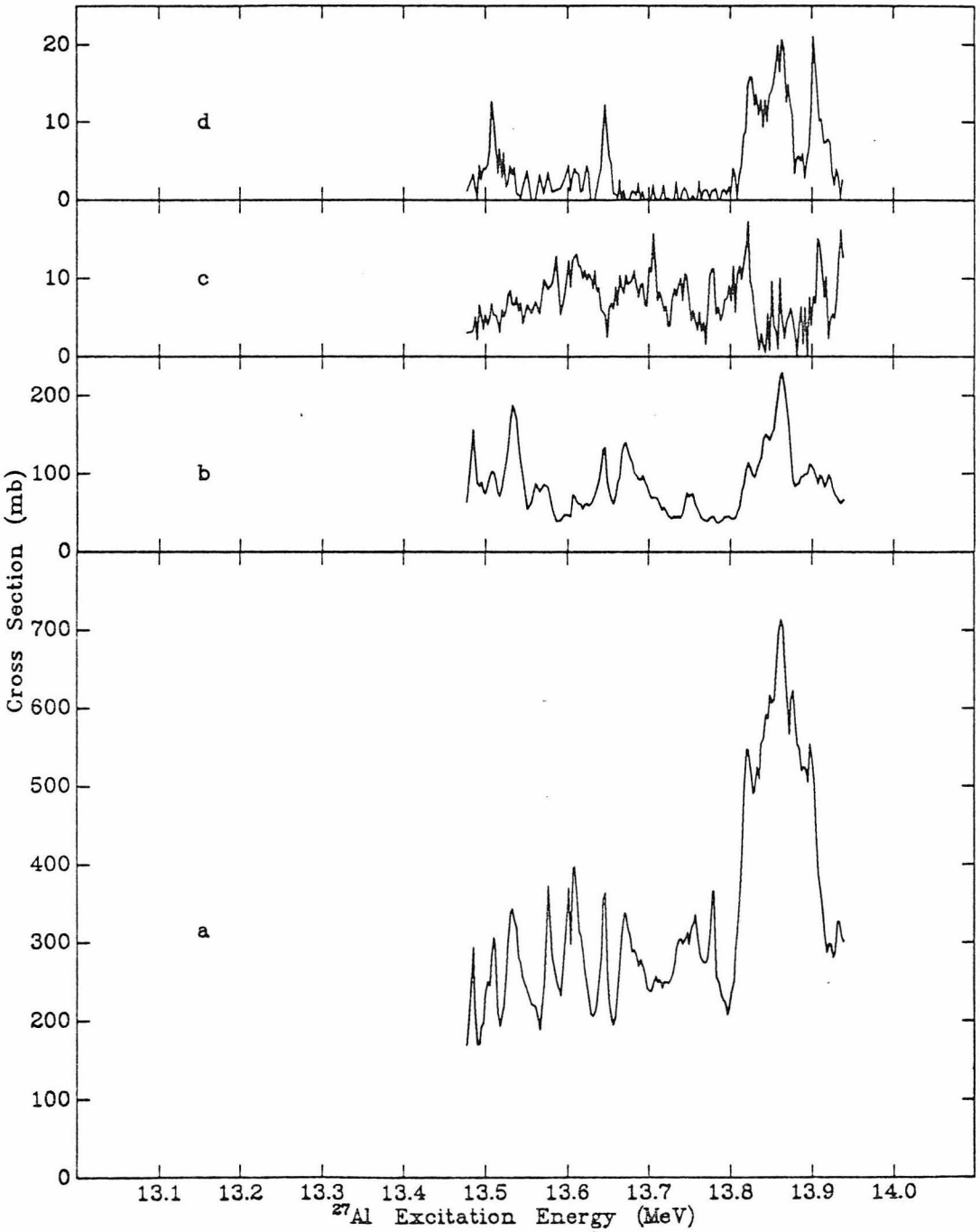
d
c
b
a
Cross Section (mb)
^{27}Al Excitation Energy (MeV)
13.1
13.2
13.3
13.4
13.5
13.6
13.7
13.8
13.9
14.0

FIGURE 32

Other Excitation Functions

Excitation functions for (a) $^{26}Mg(p,\alpha)^{23}Na^{*}$ leading to the 440-keV γ-ray; (b) $^{23}Na(\alpha,\alpha)^{23}Na^{*}$ leading to the 440-keV γ-ray; and (c) $^{23}Na(\alpha,p)^{26}Mg$ leading to the 1809-keV γ-ray.

FIGURE 32

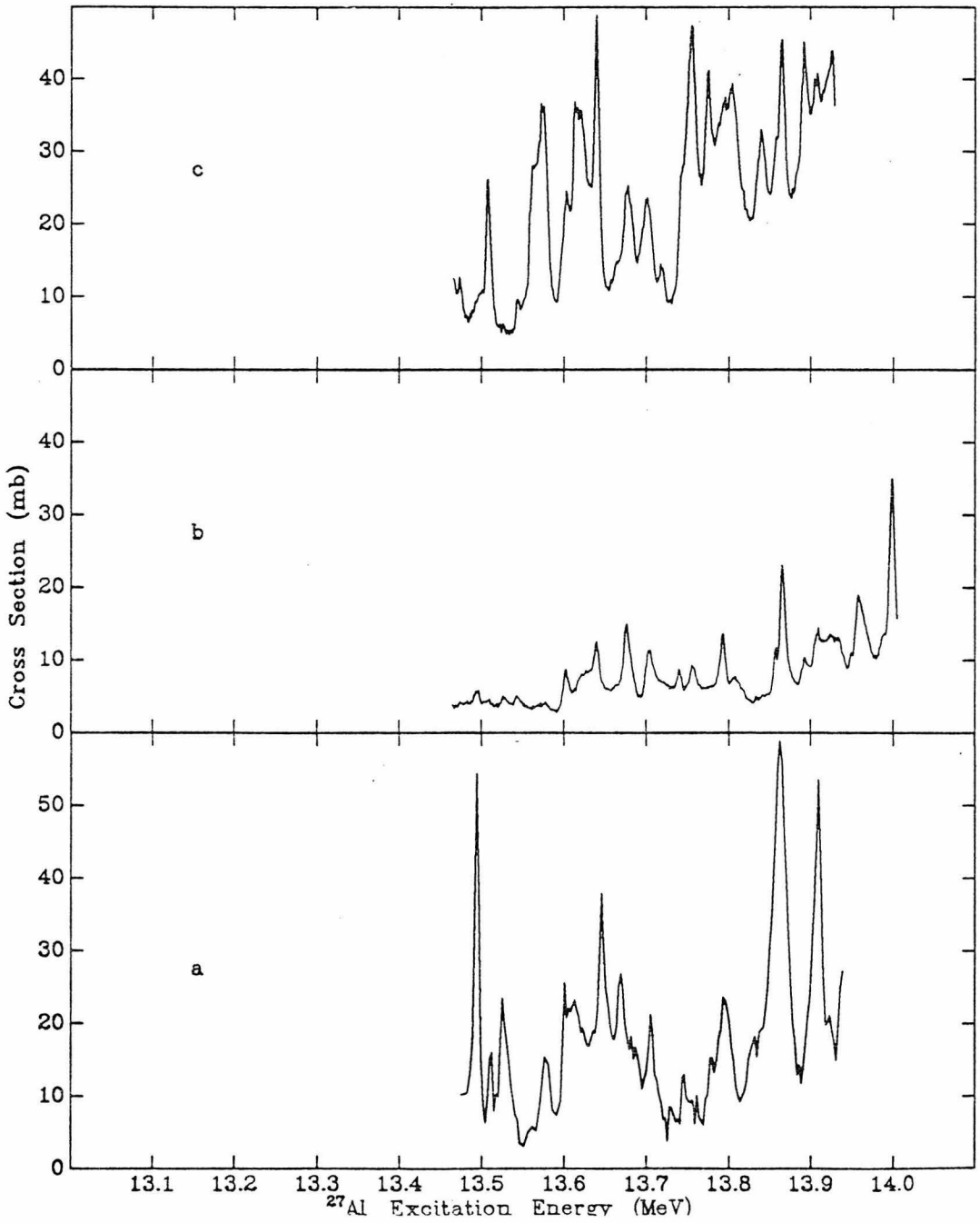
c
b
a
Cross Section (mb)
^{27}Al Excitation Energy (MeV)
13.1
13.2
13.3
13.4
13.5
13.6
13.7
13.8
13.9
14.0